# Eddy Vertical Structure and Variability: Deepglider Observations in the North Atlantic

JACOB M. STEINBERG<sup>a,b</sup> AND CHARLES C. ERIKSEN<sup>b</sup>

<sup>a</sup> Woods Hole Oceanographic Institution, Woods Hole, Massachusetts <sup>b</sup> School of Oceanography, University of Washington, Seattle, Washington

(Manuscript received 23 March 2021, in final form 10 February 2022)

ABSTRACT: Hundreds of full-depth temperature and salinity profiles collected by Deepglider autonomous underwater vehicles (AUVs) in the North Atlantic reveal robust signals in eddy isopycnal vertical displacement and horizontal current throughout the entire water column. In separate glider missions southeast of Bermuda, subsurface-intensified cold, fresh coherent vortices were observed with velocities exceeding 20 cm s<sup>-1</sup> at depths greater than 1000 m. With vertical resolution on the order of 20 m or less, these full-depth glider slant profiles newly permit estimation of scaled vertical wavenumber spectra from the barotropic through the 40th baroclinic mode. Geostrophic turbulence theory predictions of spectral slopes associated with the forward enstrophy cascade and proportional to inverse wavenumber cubed generally agree with glider-derived quasi-universal spectra of potential and kinetic energy found at a variety of locations distinguished by a wide range of mean surface eddy kinetic energy. Water-column average spectral estimates merge at high vertical mode number to established descriptions of internal wave spectra. Among glider mission sites, geographic and seasonal variability implicate bottom drag as a mechanism for dissipation, but also the need for more persistent sampling of the deep ocean.

SIGNIFICANCE STATEMENT: Relative to upper-ocean measurements of temperature, salinity, and velocity, deep ocean measurements (below 2000 m) are fewer in number and more difficult to collect. Deep measurements are needed, however, to explore the nature of deep ocean circulation contributing to the global redistribution of heat and to determine how upper-ocean behavior impacts or drives deep motions. Understanding of geographic and temporal variability in vertical structures of currents and eddies enables improved description of energy pathways in the ocean driven by turbulent interactions. In this study, we use newly developed autonomous underwater vehicles, capable of diving to the seafloor and back on a near daily basis, to collect high-resolution full ocean depth measurements at various locations in the North Atlantic. These measurements reveal connections between surface and deep motions, and importantly show their time evolution. Results of analyzing these vertical structures reveal the deep ocean to regularly "feel" events in the upper ocean and permit new comparisons to deep motions in climate models.

KEYWORDS: North Atlantic Ocean; Eddies; Mesoscale processes; Turbulence; Energy transport; In situ oceanic observations; Oceanic variability

### 1. Introduction

Energy input to the oceans through surface wind forcing, solar heating, and tides drives a large-scale circulation shaping the geographic distribution of oceanic mechanical energy, heat content, and relevant tracers. Of the dynamical processes responsible for such transport and redistribution, time-dependent mesoscale flows contain a dominant fraction of ocean kinetic energy. Manifesting as eddies, meanders, and filaments, these motions are termed balanced or quasigeostrophic (QG). This characterization reflects a dominance of planetary (f) over relative ( $\zeta$ ) vorticity (Rossby number Ro =  $|\zeta/f|$  < 1), a horizontal scale (L) of motion larger than the deformation scale  $L_d$  [Burger number Bu =  $(L_d/L)^2 < 1$ ], and flow time scales greater than ~1 day (Vallis 2006). Higher-order, unbalanced, dynamics are weaker in magnitude, but necessary to explain the evolution of mesoscale eddies and add complexity, especially at shorter space and time scales. Using newly obtained full-depth observations, this work adopts a QG framework and while the influence of unbalanced dynamics is addressed in specific cases, the main focus is to describe the vertical structure of mesoscale eddies. The term "eddy" is used here to reference density and velocity perturbations about a time mean, including those associated with coherent vortices. We explore the partition of mechanical energy (kinetic and available potential) across vertical scales, mechanisms of energy transfer across scales, and factors driving observed variability.

In the limit of unforced geostrophic turbulence, eddies are expected to equilibrate within an inertial range bounded by the submesoscale and the basin scale (10 km < L < 500 km) evolving on time scales of days to months (Charney 1971). Within this inertial range, freely turbulent interactions among flows result in the transfer of energy across spatial scales. To the extent that these motions can be described as two dimensional, Kraichnan (1967) showed that as a consequence of energy and enstrophy (vorticity squared) conservation, kinetic energy is expected to move from smaller to larger scales. Away from forcing and dissipative scales, this theory predicts a relationship between the energy spectrum E(k) and a spectral energy flux through wavenumber space, where k is horizontal wavenumber. Dimensional analysis arguments similar to Kolmogorov (1941) predict a  $k^{-5/3}$  horizontal wavenumber

Corresponding author: Jacob Steinberg, jsteinberg@whoi.edu

DOI: 10.1175/JPO-D-21-0068.1

dependence of the energy spectrum in an energy inertial range and a  $k^{-3}$  dependence in the enstrophy inertial range. Charney (1971) extended this theory to account for vertical density variations relating the energy spectrum dependence to the total wavenumber  $K^2 = k^2 + l^2 + \mu_m^2$ , where k and l are horizontal components and  $\mu_m \equiv f/c_m$  is the deformation wavenumber of the mth vertical mode (f is the Coriolis parameter and  $c_m$  is the Kelvin wave speed of the mth mode). The deformation wavenumber  $\mu_m$  is the inverse of the Rossby radius, the distance a Kelvin wave of a given vertical mode travels in an inertial time scale.

These expectations have been realized in additional theoretical and modeling work (Rhines 1979; Fu and Flierl 1980; Hua and Haidvogel 1986; Smith and Vallis 2001; Vallgren and Lindborg 2010; Kjellsson and Zanna 2017), in results estimating the horizontal kinetic energy spectra and the spectral flux of kinetic energy from observations (Scott and Wang 2005; Xu and Fu 2010, 2012), and in explaining observed eddy length scales and peak eddy energy at scales larger than that of baroclinic instability (Tulloch et al. 2009; Smith and Ferarri 2009). With the exception of a few observational datasets, however, because of the relative difficulty in obtaining deep measurements, the majority of previous work has explored QG eddy interactions and turbulence at the surface or in the upper ocean. Where vertical structure has been investigated, observations with high vertical resolution [e.g., shipboard CTD (conductivity, temperature, and depth) casts] typically have low temporal resolution and extent while those with high temporal resolution and extent (e.g., instrumented moorings) typically have low vertical spatial resolution.

Wunsch (1997) developed a key framework for describing the vertical structure of eddy kinetic energy from mooring observations using rigid-lid, flat-bottom vertical modes, but was limited in vertical resolution to the barotropic and first two baroclinic modes. These results revealed a near equal partition of energy between the barotropic and first baroclinic mode, but highlight that the sea surface height projection of interior motions is dominated by the first baroclinic mode. This interpretation was more recently revisited by de La Lama et al. (2016) and LaCasce (2017), using an expanded dataset, with results revealing vertical structure dependent on seafloor topographic slope. Authors argue that sloping-bottom modes, requiring horizontal velocity to decay with depth, more appropriately describe observed eddy vertical structure. Outside these efforts, and certain modeling analyses (Smith and Ferarri 2009), we find few attempts to explore energy partitioning among higher baroclinic modes. The following analysis revisits these conclusions and adds to the observational record of eddy vertical structure hundreds of recently collected full-depth temperature and salinity measurements with vertical resolution of order meters. We also consider spatiotemporal variability in modal energy partitioning, explored by Smith and Vallis (2001) in quantifying the role stratification plays in regulating transfers of energy across modes. Potential seasonality is inferred by Qiu et al. (2014) and Callies et al. (2015), detailing seasonality in the mixed layer and submesoscale eddy kinetic energy, a source of mesoscale eddy kinetic energy.

Eddy vertical structure, isopycnal vertical displacement and geostrophic velocity, are analyzed from full-ocean-depth measurements collected by Deepglider autonomous underwater vehicles (AUVs), hereafter referred to as gliders, between 2014 and 2019 (Fig. 1). These measurements, collected in the western North Atlantic, are analyzed to explore geographic and seasonal variability in eddy vertical structure, with observed structures interpreted predominantly through the lens of geostrophic turbulence seeking an improved understanding of the mechanisms controlling the partitioning of energy across spatial scales. To rephrase Smith and Vallis (2001), our main goal is an improved ability to explain the mechanisms determining the scale, structure, and equilibrium of mesoscale eddies. Interpreting these new measurements offers the opportunity to revisit previous observations, theory, and numerical simulation results. Section 2 describes Deepglider deployments, data collection, and construction of isopycnal vertical displacement and geostrophic velocity profiles. Section 3 details normal mode analyses, mode projections, the partitioning of energy across modes, and EOF comparisons. Section 4 presents results and implications for vertical energy transfer. Section 5 concludes with a comparison to previous results.

#### 2. Data

Deepglider is a buoyancy driven AUV capable of repeatedly profiling from the surface to 6000 m and back in approximately 1.5 days during missions lasting multiple months. Like Seaglider, measurements of temperature and conductivity are made by a SeaBird Electronics thermistor and conductivity cell aspirated by vehicle motion (Eriksen et al. 2001). Measurements are processed to calculate salinity following Pelland et al. (2013). Additional sensors measure pressure, dissolved oxygen, chlorophyll fluorescence, and optical backscatter at pilot specified intervals, typically once every 10 s in the upper ocean increasing to 60 s below 1000 m. Measurements are vertically bin averaged to a nonuniform grid with intervals selected to obtain an equal number of measurements in each average. These slant profiles have a nominal vertical resolution of 1 m over the upper 150 m, 5 m between 150 and 300 m, 10 m between 300 and 1000 m, and 20 m from 1000 m to the seafloor. Gliders also infer a depth-average current (DAC) defined as the difference between GPS-tracked overground and dead-reckoned displacement. For each profile, temperature, salinity, pressure, and location are used to compute conservative temperature, absolute salinity, and neutral density  $\gamma^n(z)$ , a continuous analog to potential density (Jackett and McDougall 1997; McDougall and Barker 2011) using local reference pressures rather than a single reference pressure often chosen as the ocean surface. Neutral density is estimated using the 1980 International Equation of State (EOS-80) with subsequent vertical displacement estimates derived from neutral density checked against equivalents calculated using Conservative Temperature, Absolute Salinity, and a local reference pressure.

Between 2014 and 2019, 10 Deepglider missions were undertaken at various sites in the western North Atlantic

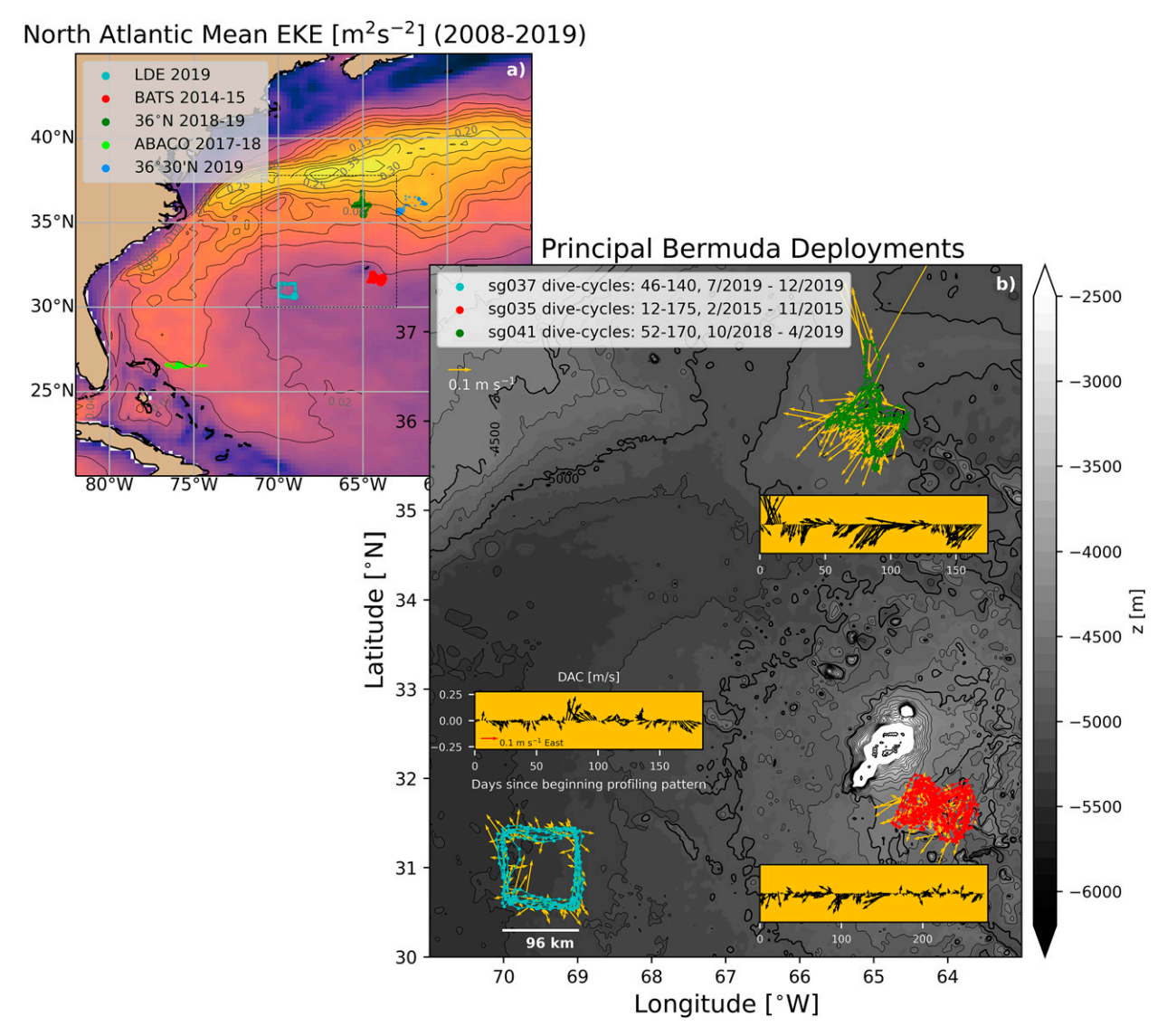


FIG. 1. (a) Five Deepglider mission sites in the western North Atlantic with mean eddy kinetic energy derived from AVISO gridded sea level anomaly fields colored and contoured. BATS, ABACO, and  $36^{\circ}N$  mission sites were visited multiple times. The dashed box locates (b). (b) Midpoint locations of dive–climb cycles completed; around station BATS in 2015 over a 10-month period (red), at  $36^{\circ}N$ ,  $65^{\circ}W$  completed in 2018 over a 6-month period (green), and at the Local Dynamics Experiment (LDE) site completed in 2019 over a 4-month period (cyan). Depth averaged current vectors from each dive–climb cycle are in yellow. Bathymetry is shaded in gray and contoured at 200-m intervals below 2000 m (z = -4500, -5000 m contoured in thick black). Inset figures show depth average current vectors as a function of time for each mission.

(Fig. 1a). Missions typically lasted between 3 and 10 months, varying in duration as a result of energy constraints, transit distances, and/or hardware failures. Study sites were selected as those meeting multiple criteria. Initially, sites repeatedly visited by oceanographic research vessels or those of historical significance were prioritized to both permit comparison of new and old observations, but also to permit the collection of concurrent temperature and salinity profiles by glider and shipboard instruments for calibration purposes. As deployments became more frequent, observations from sites associated with varied levels of mean eddy kinetic energy were

sought to explore geographic variability in eddy vertical structure. Bottom slope/roughness was a third factor considered in selecting glider mission locations. With the intention of considering the partitioning of energy across flat-bottom modes, sites with minimal topographic slope were sought. At all sites, bottom slope and roughness were calculated performing a two-dimensional least squares fit of plane to 1-min gridded bathymetry data (Tozer et al. 2019). Fits were made for a  $1^{\circ} \times 1^{\circ}$  latitude–longitude box centered at each site's centroid of all glider profile locations. Roughness was then defined as the root-mean-square difference between the fitted plane and

gridded bathymetry. Across all sites, vertical to horizontal slopes do not exceed  $\sim 500$  m per 100 km. As will be subsequently discussed, the applicability of flat-bottom or sloping-bottom modes should be based on this estimate, but also be gauged considering density and velocity profile structure.

Initial Deepglider deployment sites include the Bermuda Atlantic Time Series (BATS) station (31°40′N, 64°10′W) and the western section of the Rapid Climate Change (RAPID) array at 26°30'N between 77° and 74°W. Subsequent sites, selected to observe eddy recirculation in the North Atlantic subtropical gyre at locations of varied eddy energy, include the southern flank of the Gulf Stream extension at 36°N, 65°W and the POLYMODE Local Dynamics Experiment (LDE) site at 31°N, 69°30'W. With the exception of deployments along the RAPID array line, gliders were instructed to profile following either a repeat bow-tie or square box pattern, each roughly 100 km across, to sample within a fixed domain and observe the relatively slow passage of quasigeostrophic features. Following the designation scheme for Seagliders, individual Deepgliders are identified by "sgnnn," where "nnn" is the serial number ranging from 035 to 046 in this study.

# a. BATS site (31°40′N, 64°10′W): sg035 (2014), sg035 (2015)

Deepglider sg035 was deployed from Bermuda in March of 2014, sampling to the southeast of the island for 65 days and again in February 2015 for 276 days. For each mission, gliders collected full-depth slant profiles of temperature and salinity on a near daily basis following a repeat bow-tie pattern centered at station BATS (Fig. 1b). This pattern was selected and aligned such that the long transect arms of the bow-tie were oriented in the along-slope and across-slope direction of the Bermuda rise. A total of 114 and 326 full-depth slant profiles of temperature and salinity were completed in 2014 and 2015, respectively. Zonal and meridional bathymetric slopes are [0.005, 0.003] m m<sup>-1</sup> with a root-mean-square (rms) roughness estimate of 133 m.

# b. ABACO (26°30′N, 74°-77°W): sg037, sg038 (2017); sg037, sg039 (2018)

Deepgliders sg037 and sg038 were deployed in April 2017 from Florida and completed repeat transects along the western end of the RAPID array for approximately a 2-month period (85 and 61 days respectively collecting 70 and 60 full-depth profiles). Repeat zonal glider transects of 125–250 km were completed sampling the North Atlantic's deep western boundary current and meridional flow at the western end of the subtropical gyre (Fig. 1a). Two gliders were again deployed in 2018 from the Bahamas, for 156 and 112 days, respectively, occupying the same 250 km western section of the RAPID array. Gliders experienced meridional velocities exceeding 30 cm s<sup>-1</sup> throughout much of the water column yet experienced hardware issues limiting the calculation of isopycnal vertical displacement and geostrophic velocity. Away from the continental slope, zonal and meridional

bathymetric slopes at 75°W are [0.002, 0.0008] m m<sup>-1</sup> with an rms roughness estimate of 57 m.

# c. Gulf Stream extension (36°N, 65°W): sg041 (2018), sg045 (2019), sg046 (2019)

Deepglider sg041 was deployed from Bermuda in October 2018 and piloted to 36°N, 65°W, occupying a repeat bow-tie pattern for 177 days collecting over 250 full-depth slant profiles of temperature and salinity (Fig. 1b). This location, due south of the Gulf Stream extension, was selected to observe a highly energetic eddy field, presumably near the site of eddy formation, while maintaining the ability to pilot gliders effectively while experiencing current speeds in excess of 0.5 m s<sup>-1</sup>. Deepglider sg045 was deployed from Bermuda in June 2019 and piloted to 36°N, 65°W, where it occupied a box pattern for 56 days, completing two circuits while continuing to sample the eddy field into the summer. Rather than a bow-tie pattern, the zonally and meridionally aligned box pattern was selected to permit separate estimation of both zonal and meridional crosstrack geostrophic velocities. Zonal and meridional bathymetric slopes are [0.0003, 0.0004] m m<sup>-1</sup> with an rms roughness estimate of 60 m.

# d. LDE site (31°N, 69°30'W): sg037 (2019)

Deepglider sg037 was deployed from Bermuda in June 2019 and piloted to 31°N, 69°30′W, the location of the of Local Dynamics Experiment carried out in 1978 (McWilliams et al. 1983) (Fig. 1b). This site was selected to continue LDE surveys, but also because it is located within a region of eddy recirculation away from the Gulf Stream. A repeat box pattern was selected with 192 displacement and velocity profiles calculated from seven circuits completed in 179 days. The orientation of the box sampling pattern permits separate consideration of zonal and meridional geostrophic velocity profiles. Zonal and meridional bathymetric slopes are [0.001, 0.0003] m m<sup>-1</sup> with an rms roughness estimate of 37 m.

# e. Shipboard hydrographic records

Full-depth temperature and salinity profiles made by ship-board instruments complement glider profiles and widen the scope of eddy vertical structure analysis. While glider profiling at the Bermuda Atlantic Time Series station was initially timed to match full-depth shipboard sampling and provide reference temperature and salinity measurements, a 30-yr hydrographic record at BATS (http://bats.bios.edu/) is considered in analysis of eddy vertical structure (240 profiles). Monthly density anomaly profiles are computed relative to 30-yr seasonal background density profiles to reveal eddy isopycnal vertical displacements and mean vertical partitioning of potential energy across vertical modes. These data were collected over a time period much greater than our longest glider deployment and serve as a robust comparison to glider data.

Similar consideration of full-depth multidecade long time series at less energetic ocean stations PAPA (50°06′N, 144°54′W) (https://www.pmel.noaa.gov/ocs/Papa) (50 profiles) and ALOHA (22°45′N, 158°W) (http://aco-ssds.soest.hawaii.edu/ALOHA/) (168 profiles) in the North Pacific permit

analysis of geographic variability in vertical structure of isopycnal displacement linked to variability in dominant dynamics controlling the mean distribution of kinetic energy across scales.

### f. Glider sampling patterns

Glider profiling patterns were selected to repeatedly sample the same region while permitting the estimation of crosstrack geostrophic velocity profiles. Each segment of a bow-tie or box pattern comprises two to four dive-climb cycles completed while the glider roughly maintained a course of constant heading. Consideration of successive profiles along each bow-tie or box segment then permits estimation of an along-track density gradient. For example, at station BATS the bow-tie pattern was aligned such that cross-track velocity estimates could be made in the direction of and perpendicular to a southwestward mean flow aligning with topographic contours of the Bermuda rise (Fig. 1b).

## 1) ISOPYCNAL VERTICAL DISPLACEMENT

Displacement profiles  $\xi(z)$  are calculated relative to spatially local and temporal mean background density profiles defined as the average of all profiles collected within a certain horizontal radius and a specified time interval. Isopycnal vertical displacements about a time mean profile are interpreted as the combined influence of internal gravity waves, tides, and quasigeostrophic eddies. While these processes can be easily distinguished by their characteristic frequencies, displacement estimates calculated from individual glider slant profiles made over a multihour period alias higher-frequency signals. To address this issue, we take advantage of glider slow profiling speeds and estimate isopycnal vertical displacements and horizontal density gradients using four consecutive slant profiles collected over a multiday period (Fig. 2). At each depth, four temperature and salinity measurements are averaged to derive a single neutral density value contributing to a mean profile  $\gamma^n(z)$ . This average, computed from slant profiles completed over a time period greater than an inertial cycle averages out higher-frequency isopycnal displacements while retaining QG eddy displacements that evolve on time scales greater than the 3-day period over which the four contributing profiles are collected.

Displacements at each depth are defined as the vertical distance necessary to traverse to find the equivalent density value  $\gamma^n(z_i)$  on a long-term time average profile  $\overline{\gamma}^n(z)$ . This can likewise be defined as a local density anomaly profile divided by a local vertical density gradient profile  $\partial \overline{\gamma}^n(z)/\partial z$  such that

$$\xi(z) = \frac{\gamma^n(z) - \overline{\gamma^n}(z)}{\frac{\partial \overline{\gamma^n}(z)}{\partial z}}.$$
 (1)

## 2) GEOSTROPHIC VELOCITY

Geostrophic velocity profiles are similarly estimated from sets of four consecutive temperature and salinity profiles completed while a glider maintained a course of roughly constant compass heading. These four profiles comprise either two dive-climb or climb-dive cycles each completed over an approximate 4-day period spanning a horizontal distance of approximately 50 km. As gliders complete dive-climb cycles, small deviations in compass heading, presumed the result of variable depth-dependent currents, are ignored.

The method employed to estimate cross-track geostrophic velocity is termed the W/M method because consecutive sets of dive-climb (for W) or climb-dive (for M) cycles, used in estimating along track density gradients, appear as W or M patterns in cross section (Fig. 2). W estimation results in an estimate centered between a pair of dive-climb cycles, whereas M estimates are centered between a pair of climbdive cycles. For each set of profiles contributing to a W/M set, horizontal linear density gradients are estimated at each depth, vertical shear of the cross-track geostrophic velocity computed using thermal wind, vertical shear profiles integrated vertically, and relative velocity profiles referenced to the glider depth-average current estimate of contributing dive cycles. This technique is used to estimate absolute geostrophic velocity profiles for any set of four dive-climb or climb-dive profiles with the requirement that the glider maintains a nearconstant heading throughout the profile collection period. Horizontal, along-track, density gradients are related to vertical shear of the cross-track geostrophic velocity  $u_g(z)$  as

$$\frac{\partial u_g}{\partial z} = \frac{g}{\rho_0 f} \frac{\partial \gamma^n}{\partial x},\tag{2}$$

where x is along-track horizontal distance,  $g = 9.81 \text{ m s}^{-2}$ , and  $\rho_0 = 1025 \text{ kg m}^3$ . Profiles of vertical shear are integrated and referenced such that their depth average velocity equals the glider inferred mean depth-average current experienced during the four-profile collection period. The resulting absolute geostrophic velocity profiles are oriented perpendicular to the direction of glider flight (in the cross-track direction). Depending on piloting choices, the cross-track direction may be aligned zonally or meridionally, or at a heading that is some combination of the two. Each profile is located at the midpoint longitude and latitude of all contributing measurements (Fig. 2). More detail describing this framework can be found in Steinberg and Eriksen (2020).

# 3. Analysis framework

#### a. Normal modes, projections, and energy

The vertical structures of isopycnal displacement and geostrophic velocity are described by mode shapes  $G_m(z)$  and  $F_m(z) = dG_m/dz$ , which satisfy equivalent second order differential equations,

$$\frac{d^2G_m(z)}{dz^2} + \frac{N^2(z)}{c_m^2} G_m(z) = 0,$$
 (3)

$$\frac{d}{dz} \left[ \frac{1}{N(z)^2} \frac{dF_m(z)}{dz} \right] + \frac{1}{c_m^2} F_m(z) = 0, \tag{4}$$

derived from the primitive momentum equations after making hydrostatic and Boussinesq approximations and assuming

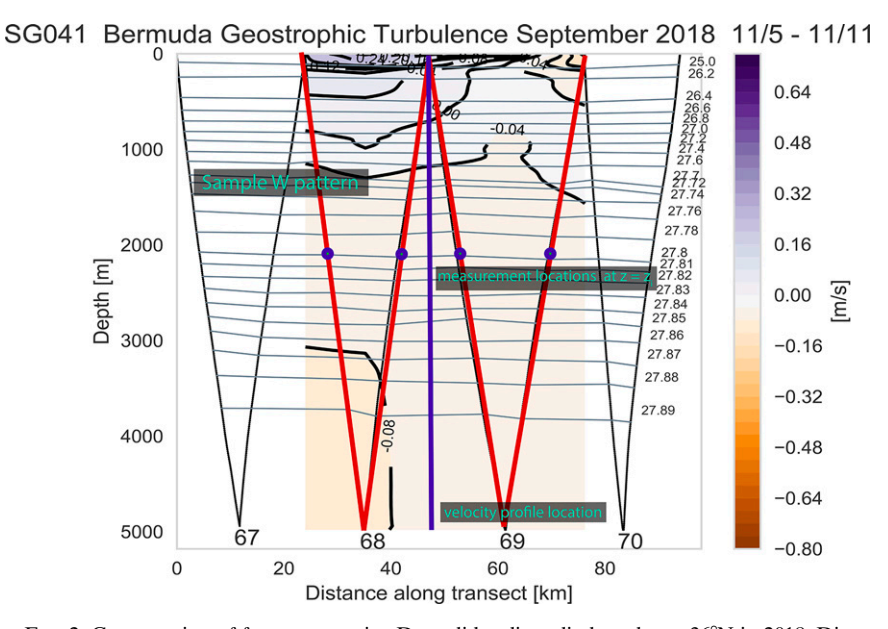


FIG. 2. Cross section of four consecutive Deepglider dive-climb cycles at 36°N in 2018. Dive-climb cycles were completed while the glider maintained a constant heading. The black sawtooth pattern identifies glider position as a function of depth and distance along transect. Neutral density contours are in gray. Colored contours are the derived cross-track geostrophic velocity field. A sample W pattern comprised of four density profiles is overlain in red and resulting cross-track geostrophic velocity profile location in dark blue.

low Rossby number flow. Here,  $N^2(z)$  is the Brunt-Väisälä buoyancy frequency, m is mode number, and  $c_m$  is the modal Kelvin wave speed. The local vertical wavenumber  $N(z)/c_m$ is independent of f while the deformation wavenumber  $\mu_m \equiv f/c_m$  varies linearly with it. Solutions are first obtained for a free surface  $[F(z=0) - (g/c_m^2)G(z=0) = 0]$  (Eriksen 1980) and flat bottom [G(z = -H) = 0]. A sloping-bottom boundary condition is also considered in the limit of horizontal velocity decaying to zero at the seafloor [F(z = -H) = 0](de La Lama et al. 2016). Termed rough-bottom modes, or more recently and extensively considered as surface modes, this basis set shows modes to generally decay with increasing depth as a function of the steepness of the bottom slope. Based on global estimates of bottom slopes, LaCasce (2017) determines these modes to be relevant across much of the globe, where slopes exceed  $10^{-3}$  m m<sup>-1</sup>, and highlights that as slopes steepen, the first baroclinic mode exhibits no zero crossing, like the first baroclinic mode in the F(z = -H) = 0limit, and the barotropic mode becomes a bottom trapped wave. These modes are subsequently solved for using the F(z = -H) = 0 bottom boundary condition, because solutions dependent on slope also vary with wavelength and angle of propagation, making them unique for all eddy features. We retain the more general solution, with the F(z = -H) = 0 bottom boundary condition, and compare these modes alongside flat-bottom modes to velocity profile structure. As noted by de La Lama et al. (2016), these solutions do not include the bottom intensified topographic mode and their use in decomposing velocity profile structure should follow the removal of topographic wave contributions to individual profiles. In

practice, removing this contribution requires knowledge of topographic mode wavelength and propagation direction. As glider observations and the analysis framework employed here cannot resolve these features, subsequent mode comparisons become dependent on both slope and observed bottom velocities.

Solution eigenfunctions form a dynamically relevant orthogonal basis set that can be then used to partition observed vertical structures across scale. Solutions for the first 40 eigenvalues  $c_m$  and eigenfunctions  $G_m(z)$  (m = 1–40) and  $F_m(z)$  (m = 0–40) for free-surface, flat-bottom, and sloping-bottom boundary conditions are obtained numerically. The zeroth index added to velocity modes represents the barotropic mode. These solutions satisfy

$$\frac{1}{H} \int_{-H}^{0} F_m(z) F_n(z) dz = \delta_{mn}, \qquad (5)$$

$$\frac{1}{H} \frac{gG_m(0)^2}{c_m^2} + \frac{1}{H} \int_{-H}^0 \frac{N^2(z)G_m^2(z)}{c_m^2} dz = 1,$$
 (6)

where  $g = 9.81 \text{ m s}^{-1}$  and H is the full ocean depth. These mode structures vary with background stratification such that higher number mode amplitude maxima and minima shoal or deepen in the presence or absence of a strong pycnocline. The effect of this stretching and squashing of mode shape increases with increasing mode number. It is well recognized that these basis functions are also useful in describing the vertical structure of internal tides and gravity waves. These unbalanced motions, however, have higher frequencies and, outside of regions with rough/steep topographic features and

excluding the mixed layer, smaller amplitudes than quasigeostrophic motions (Qiu et al. 2018).

Isopycnal vertical displacement and cross-track geostrophic velocity profiles are projected onto normalized velocity and displacement modes to determine mode amplitudes  $\alpha_m$  and  $\beta_m$  for each *i*th profile. This permits eddy vertical structure to be partitioned into contributions from each mode, each scaled by respective spatially and temporally varying amplitudes, as

$$u_i(z), v_i(z) = \sum_{m=0}^{M} \alpha_{mi} F_m(z),$$
 (7)

$$\xi_i(z) = \sum_{m=1}^{M} \beta_{mi} G_m(z). \tag{8}$$

Orientation of glider flight patterns and the method of velocity profile estimation geometrically constrain velocity profiles to represent either zonal velocities u, meridional velocities v, or some projection of the two. Glider velocities are subsequently labeled as u for convenience, unless zonal and/or meridional components were directly estimated.

Presuming little horizontal variability across a glider's sampling pattern, kinetic energy is estimated by vertically integrating the square of each *i*th geostrophic velocity profile where

$$\frac{1}{H} \int_{-H}^{0} u_i^2(z) dz = \frac{1}{H} \int_{-H}^{0} \sum_{m=0}^{40} \alpha_{mi} F_m(z) \sum_{n=0}^{40} \alpha_{ni} F_n(z) dz \tag{9}$$

where m, n are again mode number indices and the first 40 modes are considered sufficient to reproduce velocity structure derived from glider measurements. By the orthogonality of the modes, cross terms in the product of sums drop out giving a water column average modal partition of kinetic for each profile. Averaging across i profiles, mean kinetic energy as a function of mode number m and mean mode amplitudes  $\langle \alpha_m \rangle$  is

$$KE_{m} = \left\langle u^{2} \right\rangle = \sum_{m=0}^{40} \left\langle \alpha_{m}^{2} \frac{1}{H} \int_{-H}^{0} F_{m}^{2}(z) dz \right\rangle = \sum_{m=0}^{40} \left\langle \alpha_{m}^{2} \right\rangle.$$
 (10)

Because these velocity profiles, describing flow in the direction perpendicular to glider transects, are oriented across a range of compass headings dependent on glider trajectories, the zonal and meridional velocity field is presumed isotropic. Where sampling patterns permit, separate mean zonal and meridional kinetic energy is approximated as

$$KE_m = \frac{1}{2} \left( \sum_{m=0}^{40} \left\langle \alpha_{um}^2 \right\rangle + \sum_{m=0}^{40} \left\langle \alpha_{vm}^2 \right\rangle \right), \tag{11}$$

where subscripts *um* and *vm* refer to zonal and meridional mode amplitudes. Estimates of isopycnal vertical displacement are used to determine the partition of potential energy across modes. Following the normalization choices in Eqs. (5) and (6), water column average potential energy per unit mass for the first 40 modes can be written as

$$\begin{aligned} \text{PE}_{m} &= \left\langle \frac{1}{2H} \int_{-H}^{0} \xi_{i}^{2}(z) N^{2}(z) dz \right\rangle = \frac{1}{2H} \sum_{m=1}^{40} \left\langle \beta_{m}^{2} \int_{-H}^{0} F_{m}^{2}(z) c_{m}^{2} dz \right\rangle \\ &= \frac{1}{2} \sum_{m=1}^{40} \left\langle \beta_{m}^{2} c_{m}^{2} \right\rangle, \end{aligned} \tag{12}$$

taking a form similar to that derived by Oort et al. (1989). This framework then permits consideration of geographic and seasonal variability in energy partitioning across modes and hints at the mechanisms regulating this partitioning and energy pathways toward dissipation.

The relative ease or difficulty with which energy is transferred across these modes can be anticipated considering a triple interaction coefficient

$$\epsilon_{mij} = \frac{1}{H} \int_{-H}^{0} F_m(z) F_i(z) F_j(z) dz, \tag{13}$$

where m, i, and j are mode number indices and  $\epsilon_{mij}$  is a function only of background stratification. This coefficient is obtained via substitution of Eq. (4) in to the QG potential vorticity equation (Hua and Haidvogel 1986) and scales the term describing nonlinear eddy-eddy interactions. Flierl (1978) and Zhao et al. (2018) interpret this term as advection from velocity in the ith mode of potential vorticity in the  $i^{th}$  mode resulting in a change in potential vorticity in the mth mode. The interaction coefficient thus indicates the relative enhancement or inhibition of energy transfer among modes m, i, and j. Smith and Vallis (2001), using an analytical exponentially decaying background density profile, show that this interaction coefficient increases in magnitude for low baroclinic mode triplets (i, j, m = 1-3) with increasing strength of an upper-ocean pycnocline. For the same background density profile, mode triplet interaction coefficients involving the barotropic mode do not increase in magnitude. This relative increase among baroclinic mode triplet interaction coefficients corresponds to a relative enhancement of energy transfer among contributing modes and a relative inhibition of transfers to the barotropic mode. The case where m = i = j describes the mode selfinteraction, or the relative tendency for energy in a specific mode to remain in that mode. The relative partition of energy across modes can then be interpreted alongside mode triplet interaction coefficients, anticipating the relative ease or difficulty of energy transfer across modes and as a result, mean energy partitioning across modes.

## b. Vertical mode spectra

Equations (10) and (12) permit kinetic and potential energy profiles to be decomposed into contributions from each mode. Whether considered for each profile or averaged at one site over many months, this partitioning can be compared to the expectation of the predicted scaled vertical wavenumber dependence on the kinetic or potential energy spectrum. Within the enstrophy inertial range, Charney (1971) predicts this dependence to be inverse cubic for both horizontal wavenumber and deformation wavenumber  $\mu_m$ . The relevance of this prediction to glider derived spectra depends on the

assumption that gliders sample the presumed isotropic turbulence equally across all angles and that the three components of the potential vorticity behave as random uncorrelated functions. The result assumes that the total energy spectrum depends only on a fixed transfer rate across zonal, meridional, and vertical wavenumbers. This corresponds to a constant spectral slope that, while not informative of the direction of the cascade, can be useful in distinguishing QG turbulence from other regimes dominated by internal gravity waves (Garrett and Munk 1979), ageostrophic motions, or surface QG dynamics (Lapeyre and Klein 2006).

We compare glider derived vertical mode kinetic and potential energy spectra across sites and against the Charney-predicted slope, but also to that expected from the internal wave field originally empirically derived by Garrett and Munk (1979). These spectra are estimated following Munk (1981), integrating his Eqs. (9.19)<sup>1</sup> and (9.20)<sup>2</sup> over the internal wave frequency band to obtain a single vertical wavenumber spectrum for each glider mission site.

While the relationship between horizontal and vertical spectra has not been much explored observationally, at locations where submesoscale turbulence in the upper ocean energizes higher horizontal wavenumbers and flattens the energy spectra, the vertical partitioning of energy among higher modes may also be increased.

### c. EOFs

While normal modes  $[F_m(z), G_m(z)]$  reflect vertical structures implicit in the linearized quasigeostrophic potential vorticity equation, eddy vertical structure can also be considered statistically using empirical orthogonal functions (EOFs) (Emery and Thomson 1998). These functions derive from diagonalization of covariance matrices to produce orthogonal functions that reveal dominant vertical patterns of variability and their temporal evolution. Displacement and velocity profiles are expressed generally as a summation of orthogonal eigenfunctions  $\phi_n$ , each scaled by a unique amplitude. For a velocity profile time series  $U_i(z,t)$ , this takes the general form of

$$U_i(z,t) = \sum_{n=1}^{N} a_i(t)\phi_{ni}$$
 (14)

where eigenfunctions  $\phi_n$  are calculated solving the standard eigenvalue problem  $\mathbf{A}\phi = \Lambda\phi$ . The covariance matrix  $\mathbf{A} = (\mathbf{U}')(\mathbf{U}')^{\mathrm{T}}$  is composed of velocity anomalies and  $\Lambda_n$  are eigenvalues. EOF amplitudes associated with each velocity profile are then calculated as the vertical integral of each EOF multiplied by the velocity anomaly profile. Comparison between EOF and normal mode structures provides opportunity to diagnose the appropriateness of normal modes and their ability to reconstruct observed eddy vertical structure. EOF

and mode amplitude comparisons then reveal the temporal evolution of these structures and the temporal changes in mode amplitude contributions to complete eddy vertical structure.

#### 4. Results and discussion

a. Density variability and mode triplet interaction expectation

The effect of mean density profile variability across sites on eddy vertical structure is evident in comparison of select triplet interaction coefficients. This variability can be interpreted as the varied expectation of vertical energy partitioning across modes. Mean background density variability shifts the depth of mode amplitude maxima/minima by hundreds of meters vertically corresponding to differences in interactions coefficients by factors of 2-5 (Fig. 3). Comparison to a reference profile with constant stratification (not shown) similarly reveals enhanced mode triplet interactions among baroclinic modes for a realistically stratified ocean. Because this coefficient is dependent on buoyancy frequency, the self interactions of modes two and three are relatively enhanced in the summertime, suggesting that a greater fraction of energy might remain in these modes under conditions associated with enhanced upper-ocean stratification (Fig. 4). This seasonal change is most evident at station BATS. Additionally, permanent thermocline structure in the North Atlantic, with enhanced stratification at ~750 m, corresponds to increased mode triplet coefficients for modes greater than one. Interactions among modes two and higher in the Atlantic might be expected to be more significant than the same interactions near Hawaii in the Pacific.

Comparisons of triplet interaction coefficients help quantify an expectation of the relative enhancement or inhibition of energy transfer among barotropic and baroclinic modes. Figure 4 shows six coefficient magnitudes for interactions among the first three baroclinic modes at each site. These are all enhanced as compared to an ocean with constant stratification. Surface intensified stratification increases mode 1 self interaction at all sites, the same result as Smith and Vallis (2001). Of the sites considered, station ALOHA has the largest value for m = i = j = 1, suggesting it to be a site with a greater fraction of energy in mode one. Station PAPA, by far, has the largest value for m = i = j = 2, suggesting that the background stratification at this site has greater vertical structure (consistent with Fig. 3a). A significant difference is also apparent between the interactions of mode 3 with modes 1, 2, and 3 in the North Atlantic summer versus winter. At station BATS and 36°N, the self interaction coefficient of mode 3 increases by a factor of 2 or more in the summer. Similar seasonal changes are evident in interactions between mode 3 and modes 1 and 2 (Fig. 4). This suggests that mode triplet interactions vary seasonally and that in the summertime one might expect a greater fraction of energy to remain in higher modes than in the winter.

The retention of energy and increased interaction among modes one, two, and three in the summertime likewise implies

 $<sup>^{1}</sup>I_{\xi}(\omega,m) = b^{2}N_{0}N^{-1}(\omega^{2} - f^{2})\omega^{-2}E(\omega,m).$   $^{2}I_{u}(\omega,m) = b^{2}N_{0}N(\omega^{2} + f^{2})\omega^{-2}E(\omega,m), \text{ where energy density}$   $E(\omega,m) = 2\pi^{-1}f\omega^{-1}(\omega^{2} - f^{2})^{-1/2}\Big[(m^{2} + m_{*}^{2})^{-1}\Big]\Big/\Big[\sum_{1}^{\infty} \left(m^{2} + m_{*}^{2}\right)^{-1}\Big] \text{ (6.3 } \times 10^{-5}),$  b is the e-folding scale of N,  $N_{0} = 5.2 \times 10^{-3} \text{ s}^{-1}$ ,  $\omega$  is wave frequency, m is vertical mode number, and  $m_{\star} = 3$ .

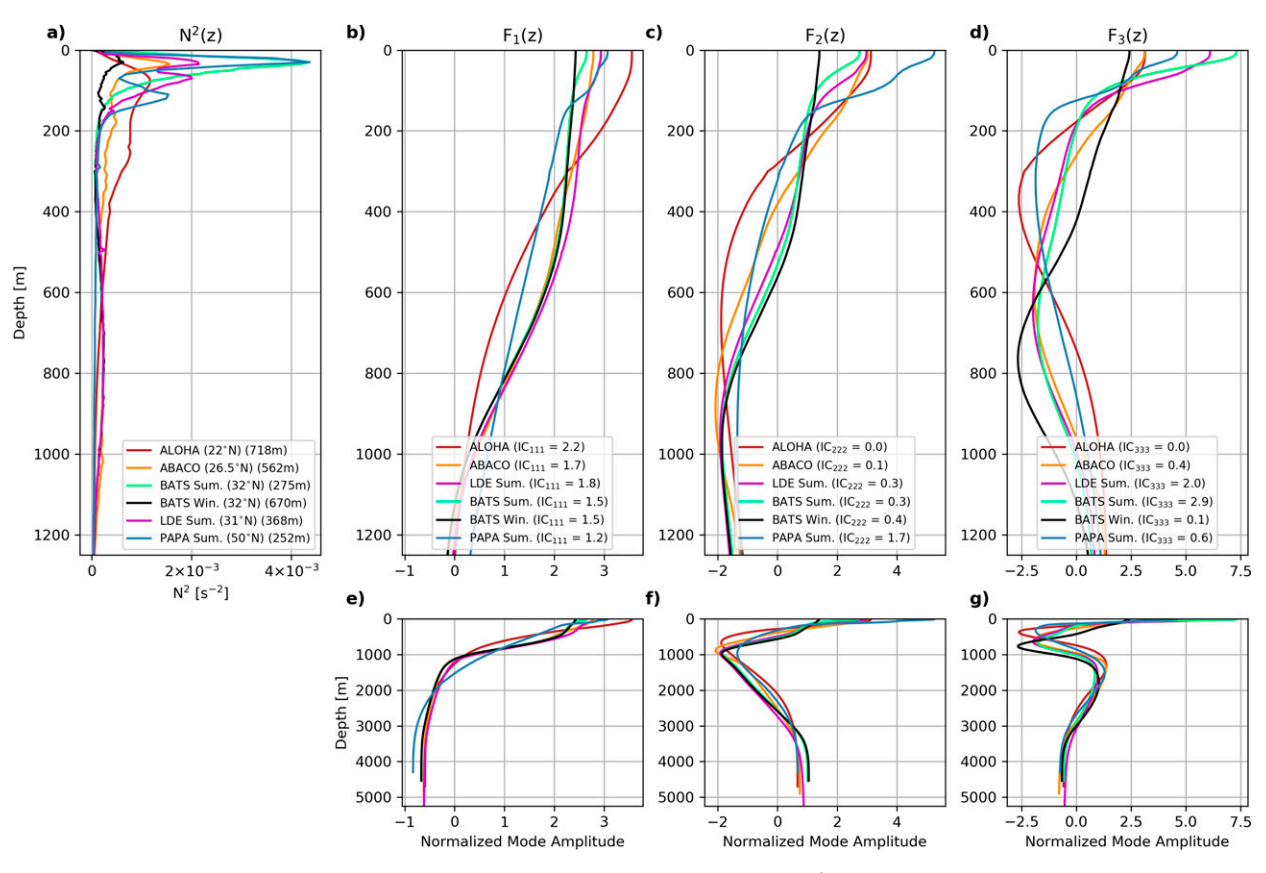


FIG. 3. (a) Mean background buoyancy frequency profiles at station ALOHA, along 26°30′N in the western North Atlantic (ABACO), at station BATS in the summer and winter, at the LDE site, and at station PAPA in the northeast Pacific over the upper 1250 m. This subset of sites was chosen to highlight the greatest variability observed in background buoyancy frequency profiles. Stratification *e*-folding depths are included in the legend. (b) First baroclinic flat bottom velocity mode at each site. (c) Second baroclinic flat bottom velocity mode at each site. (d) Third baroclinic flat bottom velocity mode at each site. (e)–(g) Full depth equivalents of (b)–(d).

a relatively reduced rate of barotropization, a result discussed by Smith and Vallis (2001) in support of observations of a peak in mesoscale eddy energy near mode one (Smith and Ferarri 2009). Without this relative inhibition of barotropization, one might expect higher mode baroclinic energy input to the eddy field at deformation radius scales to quickly barotropize and a peak in the energy spectrum to be observed at scales much larger than first deformation radii. It should be stated that comparisons among these coefficients and interpretation regarding expected energy partitioning will vary with choice of basis set used to decompose observed velocity structure.

# b. Vertical structure at station BATS

Nine-month time series of three neutral surface depths  $(\gamma^n = 27.25, 27.75, \text{ and } 28.05)$  at station BATS in 2015 reveal displacement variability at a range of frequencies and identify the passage of an individual subsurface intensified coherent vortex passing through the sampling domain in April–May 2015 (Fig. 5). This site is selected to detail because it represents the longest deployment of 276 days. The passage of the observed coherent vortex is likewise evident in satellite

altimeter derived gridded sea level anomaly estimates interpolated to glider profile locations (Fig. 5a). The correspondence between glider-following sea level anomalies and the depth of an isopycnal within the permanent pycnocline aligns with results from Wunsch (1997), that the surface primarily reflects mode 1 behavior. The correlation between glider following sea level anomaly and the depth of  $\gamma^n = 27.25$  is -0.65 at a significance level greater than 95% (Figs. 5a,b). Time series of the depths of the three selected isopycnals, calculated from both individual slant profiles as well as consecutive four-profile averages, highlight the full-depth structure of anomalies observed by altimeters at the surface and newly reveal isopycnal displacements to regularly exceed 100 m at depths greater than 2000 m.

The first 40 flat-bottom, free surface displacement and velocity modes are projected on glider displacement and velocity profiles from 2014 and 2015 deployments (Figs. 6a,b,e,f) while EOFs independently identify dominant patterns in displacement and velocity profile structure (Figs. 6d,h). The high correlation between time series of the first displacement EOF amplitude and the first baroclinic displacement mode (Fig. 5e) reveal that a dominant fraction of

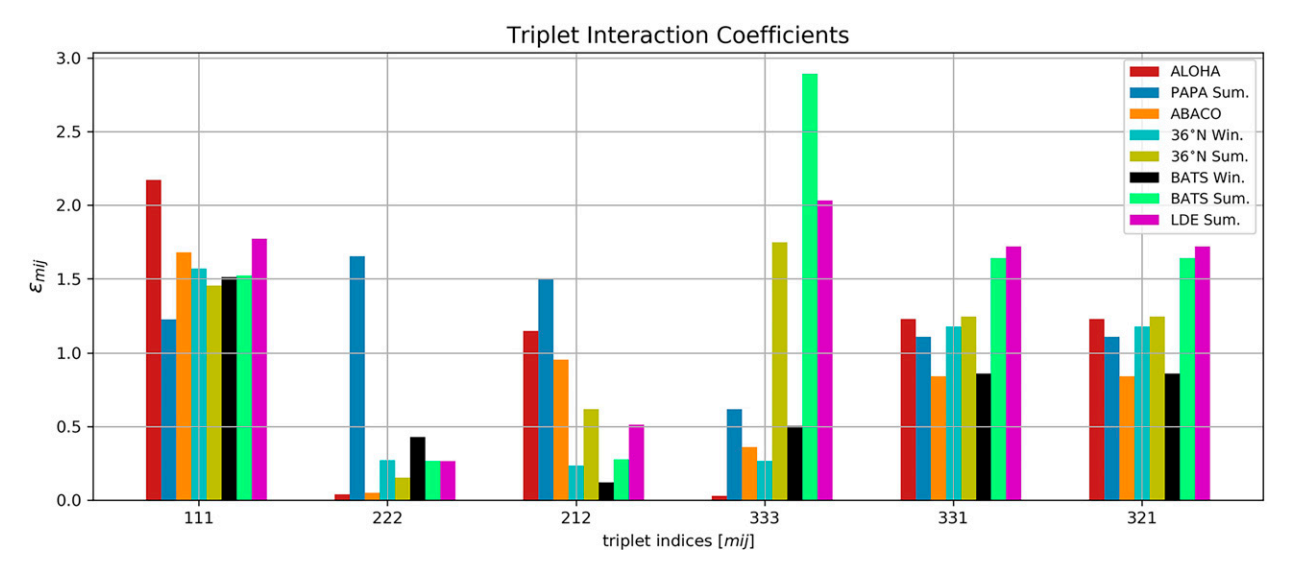


FIG. 4. Mode triplet interaction coefficients at each site for mij = 111, 222, 212, 333, 331, 321.

displacement profile variance can be explained using a single flat bottom displacement mode. Higher modes become necessary, however, in capturing the vertical structure of subsurface intensified vortices observed in both 2014 and 2015 (Figs. 6a,b,e,f, purple profiles). Velocity profiles similarly retain low mode structure, with the first three EOFs together explaining over 95% of velocity profile variance (Fig. 6d). These EOFs exhibit structures similar to both flat-bottom and sloping-bottom modes.

While the first velocity EOF decays with depth and does not change sign, similar to the first sloping bottom mode, it remains nonzero below 4200 m (blue curves Figs. 6d,h). Second and third EOFs bear resemblance to the first and second baroclinic flat bottom modes and describe 20%-40% of the velocity variance. This similarity, along with a high temporal correlation between the first displacement EOF amplitude and first flat-bottom displacement mode amplitude suggests the physical relevance of flat-bottom modes (Fig. 5e). Consideration of individual velocity profiles reveals a majority to have zero crossings at depths in the upper 1500 m, within a few hundred meters of the depth of the zero crossing of the first baroclinic flat-bottom velocity mode (Figs. 6c,g). These results, similarities between velocity EOFs and flat-bottom velocity mode structures as well as the depths of velocity profile zero crossings suggest that flat-bottom modes appropriately describe velocity profile structure.

Closer inspection and comparison of velocity profiles to flat bottom modes zero and one (barotropic and first baroclinic) as well as to sloping bottom mode one reveal temporal variability in the ability of each to explain a dominant fraction of velocity variance (Figs. 7a–d). For velocity profiles with near-zero bottom flow, the flat bottom mode reconstruction results in the cancellation of barotropic and first baroclinic amplitudes at depth (when mode amplitudes are the same sign and roughly equal in amplitude) (Figs. 7c,e). At these times the sloping bottom mode fit is better and likely more appropriate

since barotropic and first baroclinic flat bottom modes have very different phase speeds and wavelengths making it difficult to argue on their coupling. Outside of these times, however, velocities have depth-uniform nonzero structures below ~1000 m that are well described by flat bottom modes (when modal amplitudes are oppositely signed or different in magnitude) (Figs. 7a,b). It should be stated that in the limit of a flat bottom ocean, the slope-dependent solutions (LaCasce 2017) are identically the flat bottom modes, making a comparison of basis sets unnecessary. The comparisons made here then reveal the sensitivity of these basis sets to bottom slope.

It is important to note the concern of Wunsch (1997) regarding the interpretation of the first velocity EOF as a linear combination of the barotropic and first flat-bottom baroclinic mode, where this combination could then serve as evidence of modal coupling. He demonstrates that uncorrelated barotropic and baroclinic modes may appear correlated in EOF structure. Wunsch (1997) additionally notes that modes may not be orthogonal after vertical integration of samples with coarse vertical resolution, whereas EOFs are orthogonal by design. Our interpretation of EOF structure, with the aid of over an order of magnitude greater vertical resolution, focuses on nonzero near-bottom amplitudes rather than the specifics of dynamical mode coupling. de La Lama et al. (2016) and LaCasce (2017) suggest that deep velocities, like those observed here, can be described by bottom trapped topographic waves that in the limit of a flat bottom become the barotropic mode. For exponential stratification with an efolding depth of 1000 m, LaCasce (2017) quotes this transition from flat to sloping bottom mode occurring at slopes steeper than  $10^{-3}$  m m<sup>-1</sup>. While the slope at station BATS is order 10<sup>-3</sup> m m<sup>-1</sup>, the observed stratification, especially in wintertime (Fig. 3a), is more uniform and as a result shifts this expected transition slope to steeper values. The analysis framework employed here does not consider the alignment of

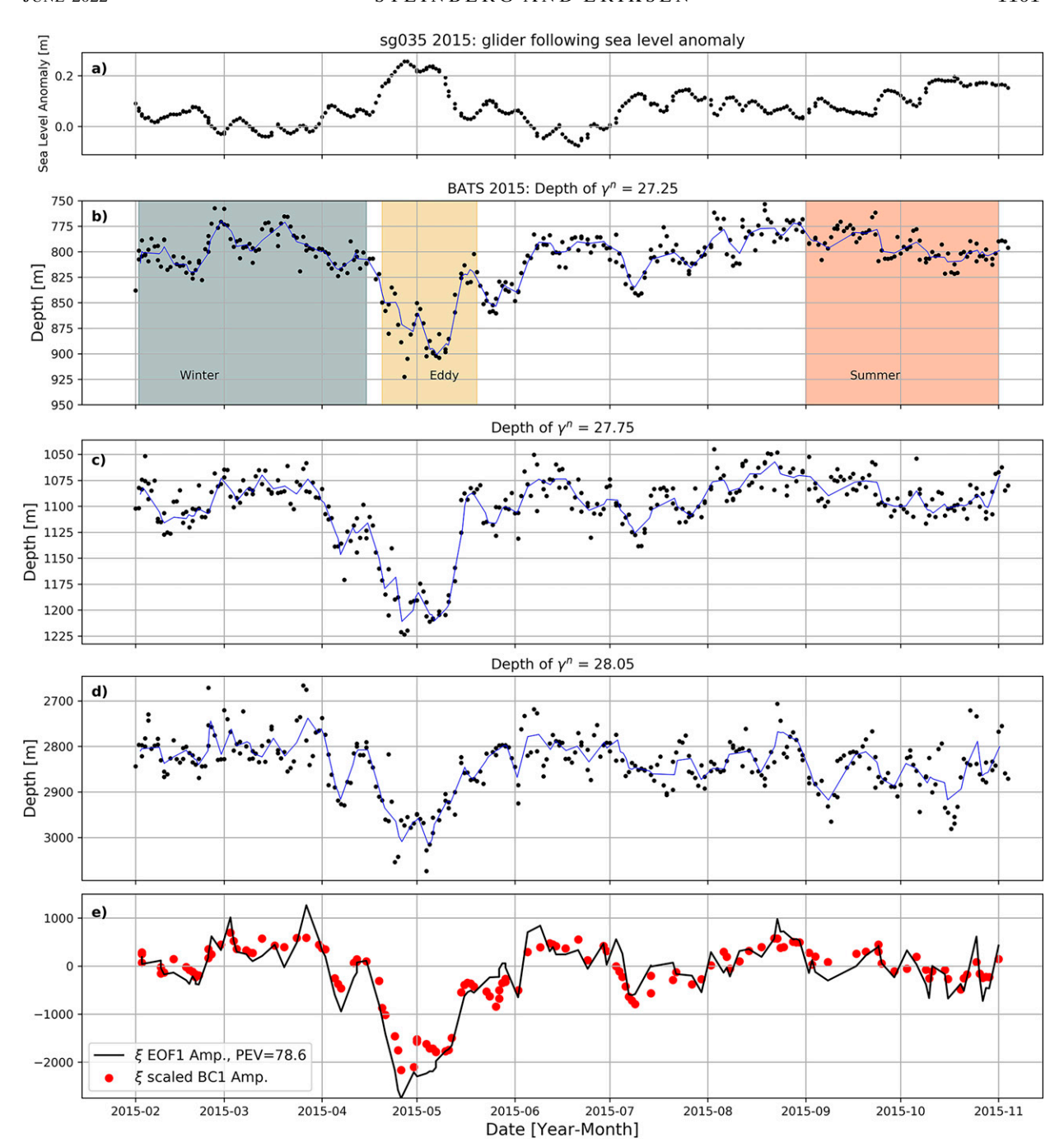


Fig. 5. (a) Time series of glider following sea level anomaly. (b)–(d) Time series of glider observed depths of three neutral density surfaces at station BATS in 2015. Shaded regions in (b) identify winter, summer, and eddy periods. Scatter points are depths from individual glider profiles while blue lines are depths from four-profile averages (used to estimate displacement profiles). (e) First displacement EOF amplitudes (black) and first baroclinic displacement mode amplitudes (red). The percent of displacement variance explained (PEV) by  $EOF_1$  is included in the legend.

topographic features nor attempt to resolve topographic waves, but to the extent that a flat-bottom approximation is satisfactory in these glider sampling regions, flat bottom modes appear appropriate and useful for this dataset in detailing the vertical structure of geostrophic turbulence.

Displacement and velocity flat-bottom mode amplitudes are then calculated with respect to seasonally varying (winter versus summer) background density profiles, and thus seasonally varying sets of modes. Mode amplitudes are averaged across seasons and separately during the passage of an

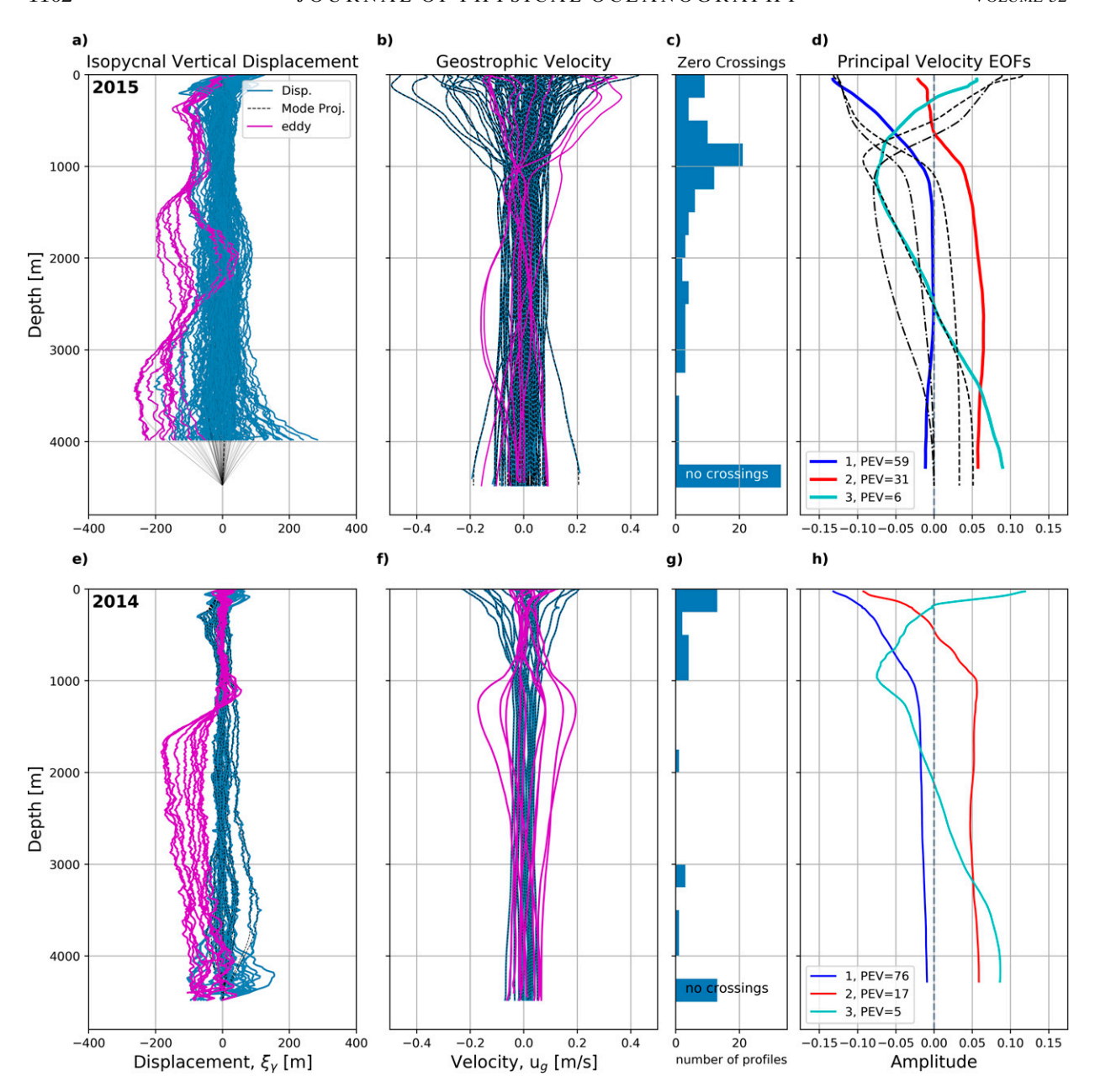


FIG. 6. (a) Glider derived isopycnal vertical displacement, (b) geostrophic velocity, (c) depths at which velocity profiles first change sign with increasing depth, and (d) first three velocity principal EOFs at station BATS in 2015 and 2014. (e)—(h) Displacement and velocity profiles of individual subsurface intensified eddies observed in 2015 and 2014 are in purple. The values labeled PEV in (d) and (h) note the percent explained eddy variance by respective EOFs calculated from all velocity profiles excluding those of the eddy. In (d), the first two flat bottom (dashed) and sloping bottom (dash—dot) velocity modes, calculated using a local background stratification profile, are added. The flat-bottom barotropic mode is excluded.

individual eddy yielding vertical wavenumber spectra that are a function of mode number (or deformation wavenumber  $\mu_m$  when scaled by f) (Fig. 8). While seasonal stratification changes occur mainly in the upper 300 m, higher mode (m > 2) structure throughout the entire water column is noticeably altered between winter and late summer (not shown). Changing with seasonality in near-surface stratification, mode three and higher

maxima and minima are shifted toward the surface in summertime and deeper in the winter (by as much as  $\sim$ 400 m). Despite this seasonal vertical shifting of mode maxima and minima, the fraction of energy contained in these higher modes is less than 10%. Among the barotropic and first three baroclinic modes, the partitioning of potential energy across modes varies between winter and summer both in eddy energy and the relative

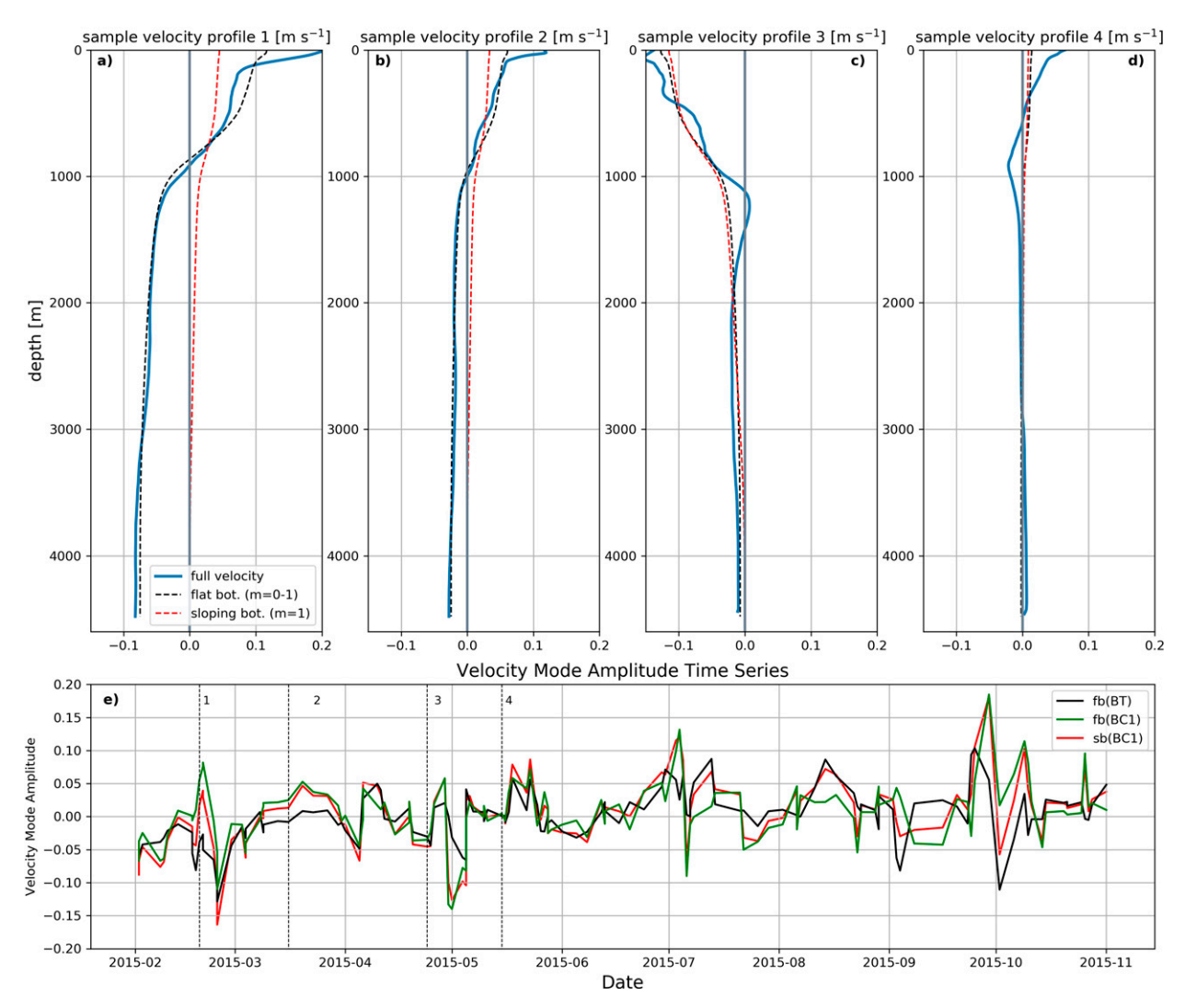


FIG. 7. (a)—(d) Four sample velocity profiles derived from measurements collected by sg035 at station BATS in 2015. Dashed lines are the reconstructed velocity profiles using the first two flat bottom (black) and first sloping bottom (red) modes. (e) Time series of flat bottom barotropic (black), flat bottom first baroclinic (green), and sloping bottom first baroclinic (red) mode amplitudes. Vertical dashed black lines are the dates of each velocity profile above.

partition across modes (Fig. 8). Aside from a decrease in barotropic energy and increase in the fraction of kinetic energy in baroclinic modes one through three in summer, the spectral slope at higher modes does not change significantly. Displacement and velocity profiles contributing to mean winter spectra were completed between February and April, while late-summer spectra were completed between September and November. These time bounds were selected to exclude the passage of the individual eddy, but also to highlight seasonal differences that would be otherwise absent if including profiles from transition periods.

Compared to summertime values, both wintertime mean kinetic and potential energy are elevated in modes one through four with a spectral slope, at modes greater than two, steeper than inverse square  $(\mu_m^{-2})$ . This pattern is consistent with a late summer decrease in satellite derived surface eddy

kinetic energy in 2015 (not shown) and with observations from Callies and Ferarri (2013), showing a wintertime increase in upper-ocean available potential and eddy kinetic energy. Mean displacement amplitude for mode one is less energetic in the late summer than in the winter by a factor of 2–3 (Fig. 8). This is coincident with a greater fraction of potential energy in modes 2–6. In winter, a greater percentage of kinetic energy is observed in the barotropic mode, while in summer, energy in the first baroclinic mode exceeds barotropic energy levels. Across higher modes, spectra maintain a seasonally independent approximately inverse cubic slope  $(\sim \mu_m^{-3})$ .

The first eight mean mode displacement amplitudes associated with the individual subsurface intensified coherent vortex are roughly an order of magnitude greater than nominal values while velocity mode amplitudes are also elevated (Fig. 8). This identifies

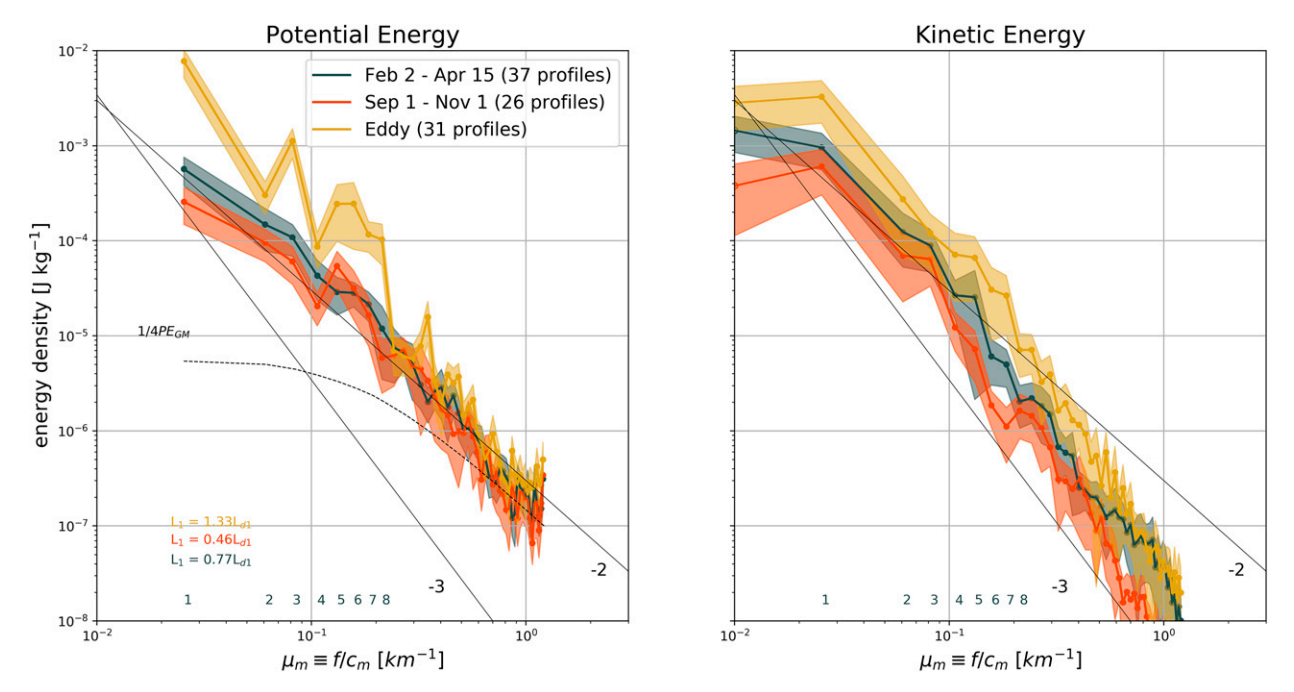


FIG. 8. Water column average potential and kinetic energy per deformation wavenumber at station BATS in 2015. Subsets of velocity and displacement profiles were selected to compare mean winter (gray), late-summer (red), and eddy (yellow) spectra. Profiles in each subset were completed within respective shaded time bounds in Fig. 5. Scattered points are labeled by corresponding mode number for the first eight baroclinic modes. The shaded regions identify 95% confidence bounds calculated using a Student's t distribution. Because profiles are not strictly all statistically independent, we estimate approximately four degrees of freedom from a roughly 2-week decorrelation time scale for displacement mode amplitudes (indirectly seen in Fig. 5d) and an approximate 2-month period over which these seasonal spectra are estimated. This implies that over the seasonal periods referred to, we observe approximately four realizations of the eddy field. The black dashed line is the empirical Garrett and Munk internal wave spectrum and solid lines are reference slopes  $\mu_m^{-2}$  and  $\mu_m^{-3}$ . A horizontal length scale  $L_1$  associated with the first mode is also predicted as  $\sqrt{\text{PE}/\text{KE}}/\mu_1$  and references eddy horizontal scales relative deformation radii. Values near to or greater than deformation radii are corroborated by Tulloch et al. (2009) and Chelton et al. (2011).

the eddy observed in 2015 as containing a significant potential energy anomaly. Displacement and velocity profiles of this feature show eddy structure extends to the seafloor, implicating bottom friction as a possibly relevant source of kinetic energy dissipation. While the presence of deep velocities suggests elevated bottom dissipation, Ruan et al. (2021), reveal its dependence on bottom slope and bottom boundary layer dynamics. This additional link between vertical structure and bathymetry suggests a landscape of dissipation dependent on eddy activity, propagation, and bottom features.

#### c. Vertical structure across sites in the North Atlantic

Displacement and velocity profiles were estimated using all available profiles at each mission site (Fig. 1) and projected onto flat-bottom displacement and velocity modes. The rms isopycnal vertical displacement and geostrophic velocity are estimated, compared across sites, and against EOFs (Fig. 9). First velocity EOF comparisons across sites (Fig. 9d) reveal marked similarities in their decay with depth to nonzero values, with the exception of Gulf Stream and ABACO sites where the first EOFs change sign at roughly 1000 m. Second velocity EOFs are also similar with nearly all changing sign at roughly 1000 m and appearing similar to the first baroclinic flat bottom mode (Fig. 9e).

At each site, we observe regular displacements of order hundreds of meters at depths greater than 2000 m. These are particularly evident during the passage of subsurface intensified eddies observed at station BATS. The vertical structure of the 2014 feature's geostrophic velocity, with greatest speeds at ~1300 m (Fig. 6f), can be explained as a combination of barotropic and second baroclinic mode structure. Peak speeds approach 0.2 m s<sup>-1</sup> and decay with depth to ~0.05 m s<sup>-1</sup> at the seafloor. Similarly, a dominant fraction of the eddy potential energy is contained in the second baroclinic mode (not shown). One difference observed in this feature, as compared to the 2015 eddy, is the lack of a surface density anomaly or strong surface velocities. Isopycnal vertical displacements (Fig. 6e) below the core depth approach 200 m in amplitude and decay with increasing depth to an average amplitude of ~100 m at the seafloor again suggesting a relevant role of bottom friction in energy dissipation.

Compared to those at station BATS, the structure of profiles completed along the 26°30′N ABACO line can be attributed to sampling much closer to a western boundary current system. At this site, northward surface flows join with waters moving through the Florida Strait to become the Gulf Stream while deep velocities are associated with deep western boundary current southward flow. Along the repeatedly profiled zonal

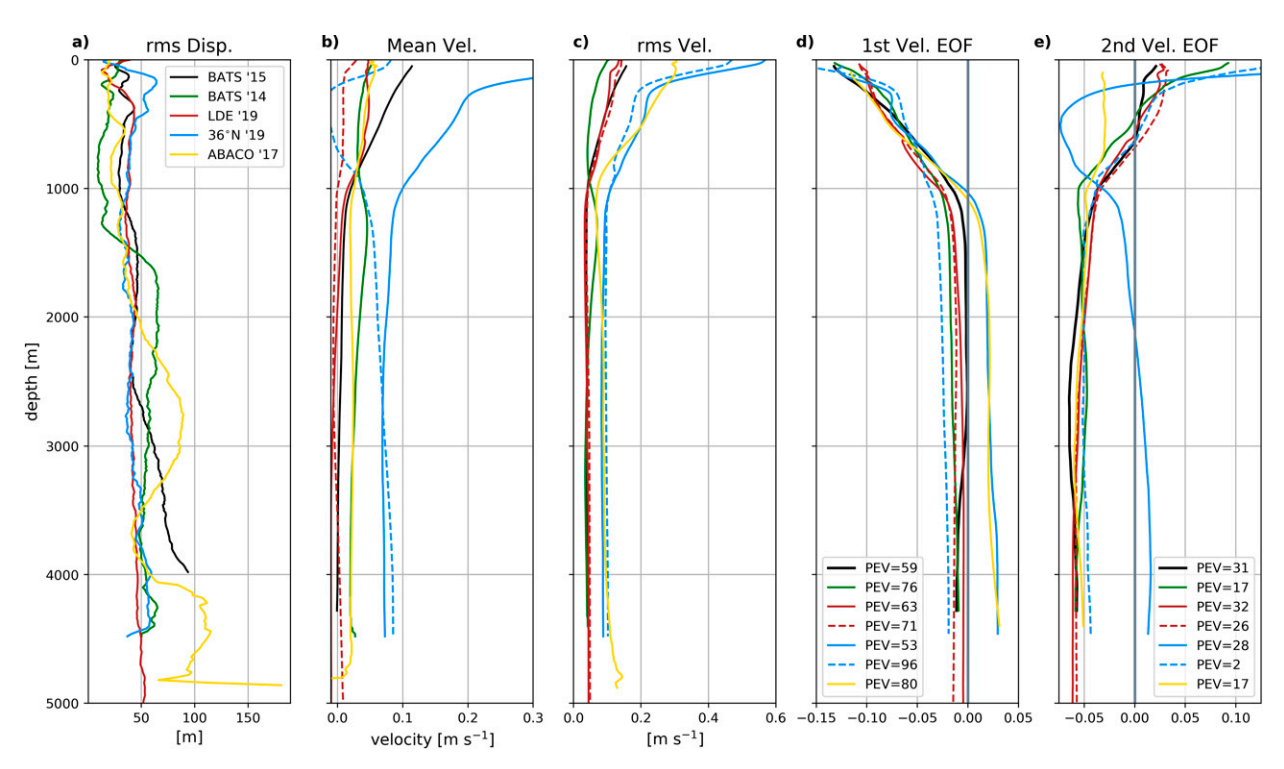


FIG. 9. (a) Root-mean-square isopycnal displacement at each site. (b) Mean cross-track geostrophic velocity. (c) Root-mean-square cross-track geostrophic velocity. (d) First principal velocity EOF. (e) Second principal velocity EOF across all mission sites. Where applicable (LDE, 36°N sites) mean velocity profiles are split into zonal (solid) and meridional (dashed) components. Percent explained variance for the first two EOFs are labeled PEV.

transect, Deepgliders sampled mean flows at the western end and a turbulent eddy field at the eastern end, similar to that observed at station BATS and the LDE site. Compared to profiles from station BATS, geostrophic velocities are generally greater in magnitude throughout the water column. Velocities at depths greater than 4000 m regularly exceeded 0.1 m s<sup>-1</sup> while surface velocities approached 0.5 m s<sup>-1</sup> (Fig. 9c). Coincident with these deep velocities is relatively larger rms displacement (Fig. 9a) that, along the western end of the transect, closer to the slope, may reflect topographic mode activity.

Sampling along the southern flank of the Gulf Stream Extension amidst enhanced eddy activity, displacement profiles from Deepglider sg041 at the 36°N site also reveal ~100-m departures from a mean background density profile throughout the water column. Depth-averaged velocities consistently to the southwest (arrows in Fig. 1b) align with altimeter derived surface velocities of ten of centimeters per second (not shown) and are suggestive of the return "eddying" circulation of the North Atlantic subtropical gyre. Compared to station BATS, surface and deep velocities are stronger, regularly exceeding 0.15 m s<sup>-1</sup> at depths greater than 2000 m (not shown). Collected at the same site one year later, Deepglider sg045 profiles similarly reveal speeds of well over 0.1 m s<sup>-1</sup> at depths greater than 2000 m (Fig. 9b). Because of a different sampling pattern geometry selected for sg045 in 2019, velocity profiles can be separated in zonal and meridional groups and separate EOFs computed to test the

assumption of horizontal isotropy (Figs. 9b–e). EOFs of zonal and meridional velocities respectively reflect first flat bottom and sloping bottom baroclinic modes. One noted difference between zonal and meridional EOF structure is the 96% fraction of variance explained by the first EOF of meridional velocity (Fig. 9d). The first two zonal velocity EOFs appear as the normal first and second baroclinic modes followed by a third EOF, describing almost 20% of velocity profile variance, that appears near barotropic. This suggests a lack of horizontal isotropy of the geostrophic velocity field, but may be expected due to the proximity to the eastbound Gulf Stream and westbound return circulation.

Finally, isopycnal vertical displacement and geostrophic velocity profiles estimated from measurements at the LDE site reflect low mode, slowly evolving quasigeostrophic features to a greater extent than the other sampling sites. This site was selected to observe the QG eddy field well within the "eddy" recirculation of the North Atlantic, but also to overlap with the region originally sampled multiple decades ago first revealing the richness in mesoscale eddy structure (McWilliams 1989). The sampling domain occupies a relatively flat region, with a bathymetric slope generally flatter than ~100 m/100 km, and is hundreds of kilometers removed from the Gulf Stream and prominent or rough bathymetric features. Away from regions generally associated with various types of instability and away from rough topography, eddy activity at this site may best reflect equilibrium QG dynamics.

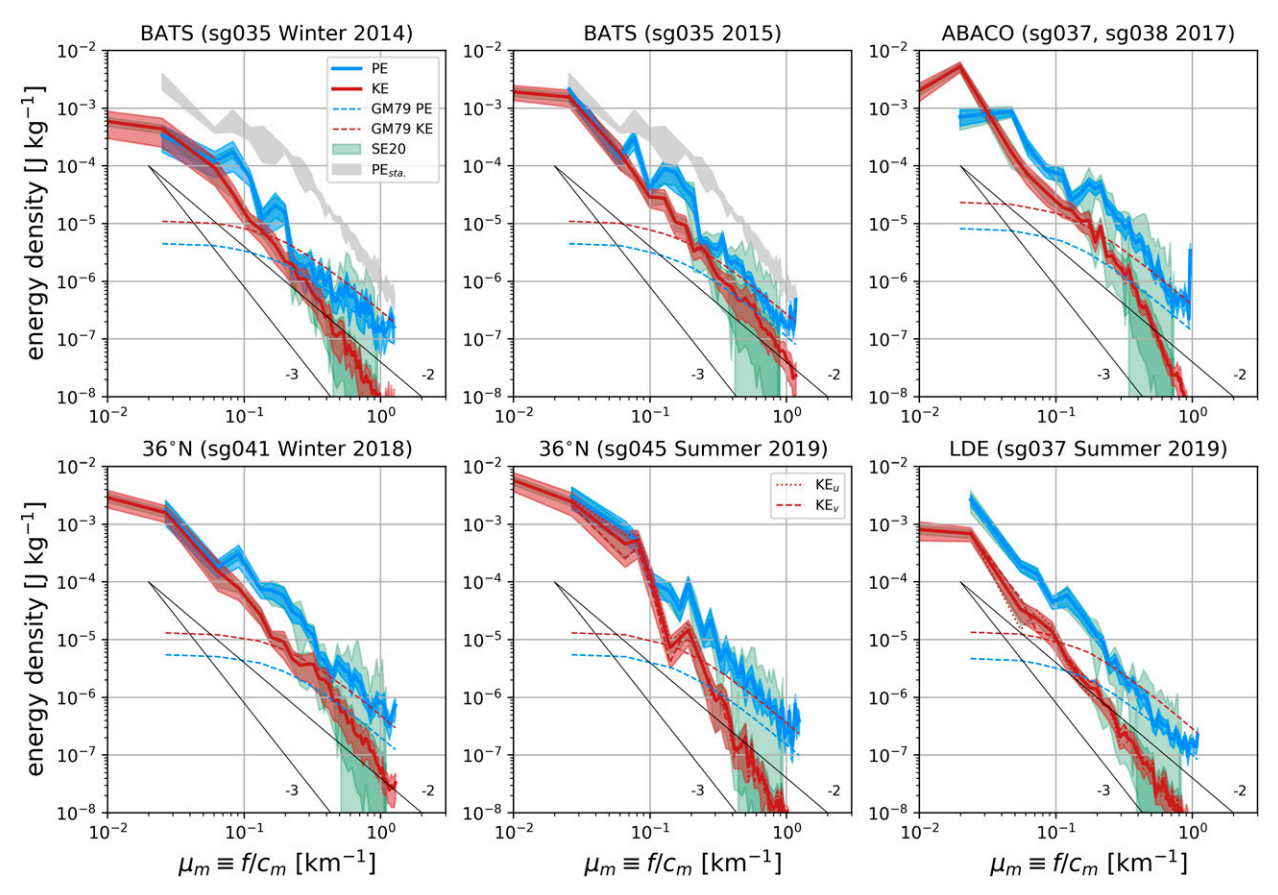


Fig. 10. Water column average potential (blue) and kinetic (red) energy per deformation wavenumber  $\mu_m \equiv f/c_m$  at each site in the western North Atlantic. The 95% confidence bounds, calculated using a Student's t distribution (von Storch and Zwiers 2003), are shaded. Light green bands are separate error bounds from Steinberg and Eriksen (2020) calculated as the difference between simulated glider and model vertical spectra and expressed as a fraction of glider estimates. In effect, this is a confidence bound determined from equivalent model spectra. These estimate bounds within which gliders can be expected to resolve vertical structure of associated modes. Kinetic energy in the barotropic mode is plotted along the vertical axis. Garrett and Munk internal wave spectra are dashed (Garrett and Munk 1979). Reference slopes of  $\mu_m^{-2}$  and  $\mu_m^{-3}$  are in solid black. Where glider sampling geometry permitted (36°N 2019, LDE 2019) dash and dash–dot lines correspond to zonal and meridional velocity components.

These factors also arguably make the use of flat-bottom modes most appropriate, as compared to the other sampling sites.

# d. Comparisons of the partitioning of energy across modes

Throughout the western North Atlantic, mean potential and kinetic energy spectra generally exhibit more similarities than differences. The wavenumber spectra appear quasi-universal (Fig. 10). With the exceptions of ABACO and the LDE site, potential and kinetic energy is nearly equipartitioned in the first and second baroclinic modes. However, among higher modes, potential energy dominates by a factor of 2 or higher. At the ABACO site, the increased fraction of kinetic energy in the first baroclinic mode can be attributed to the proximity of measurements to the western boundary current, where susceptibility to baroclinic instability may be higher. Away from the western boundary current and within a region of eddy recirculation, at the LDE site we observe potential energy to exceed kinetic across all modes. This

implies eddy length scales to be larger than local deformation radii, a predicted effect of geostrophic turbulence and the inverse cascade where energy moves from deformation radius or instability scales to larger scales.

Across all sites and all years, both potential and kinetic energy spectra exhibit a spectral slope steeper than inverse square and not significantly different than the predicted inverse cubic slope associated with the forward enstrophy cascade of geostrophic turbulence (Charney 1971). Among the barotropic and roughly first 10 baroclinic modes, spectra at each site are more energetic than those expected if internal waves were the dominant dynamics. At most sites, however, potential energy and predicted internal wave spectra converge at high wavenumber (approximately mode 20 or higher) with an inverse square slope. This result suggests internal wave dynamics to dominate at these smaller vertical scales.

Differences across sites may reflect the local or nonlocal generation of observed eddies and the strength of an inverse cascade. Altimetric observations generally report eddy length scales everywhere larger than first deformation radii with this result at least partly interpreted as evidence of an inverse energy cascade of kinetic energy to horizontal scales larger than that of the first deformation radius (Chelton et al. 2011). At sites farther from presumed locations of eddy generation (i.e., the Gulf Stream Extension), such as the LDE site, the dominance of potential energy to kinetic implies eddy length scales to be greater than the first deformation radius. Among higher modes and across all mission sites, horizontal eddy length scales are inferred to be at least a factor of 2 larger than the modal deformation radii.

Kinetic energy within each mode varies across sites by roughly an order of magnitude. At the upper end of this distribution are 36°N and ABACO, as might be expected for their proximity to the Gulf Stream and deep western boundary current, respectively. These sites are characteristically more energetic as a result of their proximity to boundary currents. The BATS site in 2014 and the LDE site, on the other hand, are least energetic, as might be expected due to their location away from sites of increased eddy activity. Interestingly, potential energy in mode one at the BATS site in 2015 and the LDE site is nearly equal to that at 36°N in 2019. While these sites generally exhibit relatively less eddy activity, increased levels of mode one potential energy may be explained as a result of the inverse cascade in an ocean with surface intensified stratification.

Comparisons of the modal partitioning of mean potential energy at stations BATS, PAPA, and ALOHA demonstrate that spectra computed from observations collected in both the Atlantic and Pacific decay with increasing mode number in a similar manner. As expected, station BATS is the most energetic at low modes with the steepest spectral slope among the three sites (Fig. 11). These spectra all converge at approximately mode 20, are roughly equally energetic through mode 60, and maintain a spectral slope steeper than inverse square between modes 11 and 60. Empirically derived internal wave potential energy spectra of Munk (1981) intersect each site's spectrum at approximately mode 30, implying that at lower modes, isopycnal vertical displacements are greater than would be expected by internal gravity waves alone. This displacement variance identifies the passage of quasigeostrophic eddies. Vertical scales and deformation radii decrease with increasing mode number such that at modes 20 and higher horizontal scales are less than ~5 km. Motions at these comparatively small scales may reflect internal waves and nonlinear dynamics such that assumptions of quasigeostrophy employed to analyze eddy vertical structure become inadequate. Among low modes, however, comparison among stations shows BATS to be the most energetic due to its proximity to the Gulf Stream, followed by stations ALOHA and PAPA. Across all modes, the spectrum at station PAPA, a site in the northeastern Pacific associated with little quasigeostrophic eddy energy, is closest to the predicted internal wave spectrum in both magnitude and slope.

### 5. Summary and conclusions

Deepglider missions in the western North Atlantic carried out over 5 years provide near daily observations of full-depth

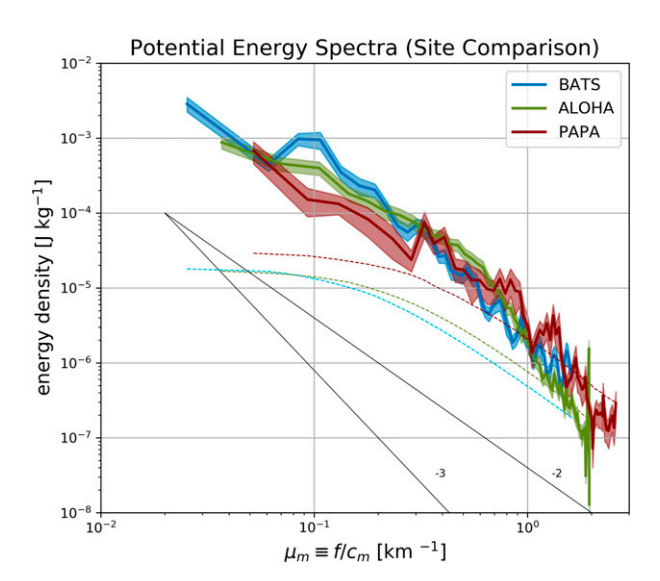


FIG. 11. Potential energy per deformation wavenumber at stations BATS, ALOHA, and PAPA from hydrographic data (shipboard instruments). Colored dashed lines are the corresponding Garrett and Munk internal wave spectra. Solid black lines reference inverse square and inverse cubic slopes. Shaded bands are 95% confidence intervals calculated using a Student's *t* distribution from 240, 168, and 50 profiles at each respective site. The offset among spectra along the horizontal axis reflects varying deformation radii for each mode at each site due to changes in latitude and stratification.

eddy structure and variability from which vertical wavenumber spectra of potential and kinetic energy are estimated. Partitioning of mechanical energy across vertical modes has only previously been considered for coarsely resolved observations resolving low mode structure and in numerical simulations (Smith and Ferarri 2009). The increase in vertical resolution that these profiles provide permits projections onto the barotropic and first 40 baroclinic modes and enables an analysis of spectral slopes of potential and kinetic energy. Across all sampling sites, observations are consistent with an expected forward enstrophy cascade from larger to smaller vertical scales. Vertical wavenumber spectra of geostrophic motions vary as  $\mu_m^{-3}$ , consistent with the predictions of geostrophic turbulence (Charney 1971). Isopycnal vertical displacements of order 200 m, at depths greater than 2000 m, reveal mesoscale eddy vertical structure to regularly extend to the seafloor. In both 2014 and 2015, subsurface intensified eddies were observed at station BATS with cold, freshwater mass anomalies suggesting their origin to be the Labrador Sea (Bower et al. 2013). The surface expressions of these features were markedly different between the two years, implying the inadequacy of altimetric sea level anomaly observations in their ability to detail subsurface intensified eddy structure. These isolated coherent eddies in the western North Atlantic extend throughout the water column. The extent to which these eddies are altered by topographic features is poorly understood, yet new observational efforts (Andres et al. 2020), along with these results, suggest their effect on abyssal flows to be nonnegligible.

Mode triplet interactions characterize a mechanism by which energy is transferred across vertical scales. These results suggest that such interactions vary seasonally in response to seasonal changes in upper-ocean stratification such as to enhance energy in higher baroclinic modes in the summer versus winter. These interactions are expected to be enhanced among higher modes for mean density profiles with enhanced near-surface stratification. The relative structures of seasonal and permanent thermoclines can increase the relative importance of higher baroclinic mode triplet interactions and the retention of higher mode energy in higher modes. Increases in near-surface stratification thus result in an increase in the relative modal partition of energy among higher modes, as was observed at station BATS in 2015 with a summertime shift to a flatter potential energy spectrum across modes one through five. In comparing flat and sloping bottom modes alongside topographic slope estimates at each site, we find the flat bottom assumption enables dynamically relevant adequate reconstruction of velocity profiles and empirical orthogonal functions of geostrophic eddy motions. Outside of the ABACO and 36°N sites, the first velocity EOF (describing ~50%-90% of the variance) generally decays with depth, but nonzero velocities with near uniform depth structure below 1000 m, display an imprint of flat bottom baroclinic mode structure. Differences across these sites may be attributed to some combination of proximity to sites of baroclinic instability (i.e., nearer to the Gulf Stream Extension) as well as the relevance of topography (i.e., proximity of BATS to the Bermuda Rise) where sloping bottom modes may become more relevant. We recognize the relevance of sloping-bottom modes (LaCasce 2017), especially in incorporating a bottom slope and implying a preferred wavenumber and direction of wave propagation, but here employ the more general flat-bottom boundary condition because their generality enables like comparisons across mission sites that all have a bottom slope order  $10^{-3}$  or shallower. These sites also have finer-scale stratification in the upper 500 m that seasonally weakens, altering the expectation of bottom slope necessary to shut down deep flow. Frequent observations of nonzero geostrophic velocities throughout the deep ocean invite questions of barotropic mode contributions and/or bottom trapped wave expectations that all motivate the need for continued high-resolution observations at locations of varied bathymetric slope and roughness. Potential energy vertical wavenumber spectra derived from long-term hydrographic observations at specific sites (stations BATS, ALOHA, and PAPA) also vary as  $\mu_m^{-3}$  for high modes, but at levels higher than those found from Deepglider surveys and ascribable to different averaging schemes. Among modes 1-10, station PAPA is the least energetic, followed by ALOHA, and then BATS. This order matches the order of mean eddy kinetic energy associated with each site. Notably, the PAPA spectrum is little more energetic than the Garrett and Munk internal wave spectrum (Garrett and Munk 1979). At station BATS and at sites north of Bermuda on the Gulf Stream flank, potential and kinetic energy are roughly equal in the first and second baroclinic modes. Across all sites, spectra are most energetic at low modes, decreasing with increasing wavenumber following a linear slope proportional to  $\mu_m^{-3}$ (that predicted by geostrophic turbulence theory). These observations compare favorably with estimates of upper-ocean horizontal

wavenumber spectra (Callies and Ferarri 2013) as well as vertical wavenumber spectra from quasigeostrophic simulations (Smith and Ferarri 2009). Variance at low modes is much greater than that produced by internal waves (Garrett and Munk 1979) because the W/M displacement and velocity profile estimation technique serves as a low-pass filter smoothing density and velocity perturbations with time scales shorter than ~2 days and spatial scales of less than ~20 km.

These high-resolution observations of full-depth geostrophic eddy structure at various sites in the western North Atlantic offer a revised look at the geography and temporal variability of the partitioning of eddy energy throughout the water column. Understanding of this partitioning continues to be important considering pathways of eddy energy into and out of the mesoscale. With the mesoscale containing a dominant fraction of ocean kinetic energy, tracing a pathway to dissipation remains necessary to improve predictions of the fate of oceanic tracers and heat.

Acknowledgments. This work was funded by NSF Grant 1736217 and would not have been possible without the help of Kirk O'Donnell, James Bennett, Noel Pelland, and all contributors to Deepglider development. We additionally thank the captain crew of the R/V Atlantic Explorer and the BATS team at the Bermuda Institute of Ocean Sciences, particularly Rod Johnson, as well as Seakeepers International for their professionalism, capability, and generous assistance in deploying and recovering gliders. Presentation and interpretation of these results benefited enormously from the assistance and advice from reviewers for which we are extremely grateful.

Data availability statement. All measurements collected by each glider are all available on the N.O.A.A. National Centers for Environmental Information Ocean Archive System: sg035 (BATS 2014; Eriksen 2017a), sg035 (BATS 2015; Eriksen 2017b), sg037 and sg038 (ABACO 2017; Eriksen 2017c), sg041 (36°N; Eriksen 2021), sg045 (36°N 2018; Eriksen 2021), sg037 (LDE 2019; Eriksen 2021).

### REFERENCES

Andres, M., and Coauthors, 2020: Eddies, topography, and the abyssal flow by the Kyushu-Palau ridge near Velasco Reef. *Oceanography*, 32, 46–55, https://doi.org/10.5670/oceanog. 2019.410.

Bower, A., R. Hendry, D. Amrhein, and J. Lilly, 2013: Direct observations of formation and propagation of subpolar eddies into the subtropical North Atlantic. *Deep-Sea Res. II*, 85, 15– 41, https://doi.org/10.1016/j.dsr2.2012.07.029.

Callies, J., and R. Ferarri, 2013: Interpreting energy and tracer spectra of upper-ocean turbulence in the submesoscale range (1–200 km). J. Phys. Oceanogr., 43, 2456–2474, https://doi.org/ 10.1175/JPO-D-13-063.1.

——, R. Ferrari, J. M. Klymak, and J. Gula, 2015: Seasonality in submesoscale turbulence. *Nat. Commun.*, 6, 6862, https://doi. org/10.1038/ncomms7862.

Charney, J., 1971: Geostrophic turbulence. *J. Atmos. Sci.*, **28**, 1087–1095, https://doi.org/10.1175/1520-0469(1971)028<1087: GT>2.0.CO:2.

- Chelton, D., M. Schlax, and R. Samelson, 2011: Global observations of nonlinear mesoscale eddies. *Prog. Oceanogr.*, 91, 167–216, https://doi.org/10.1016/j.pocean.2011.01.002.
- de La Lama, M. S., J. LaCasce, and H. Fuhr, 2016: The vertical structure of ocean eddies. *Dyn. Stat. Climate Syst.*, 1, dzw001, https://doi.org/10.1093/climsys/dzw001.
- Emery, W., and R. Thomson, 1998: *Data Analysis Methods in Physical Oceanography*. Pergamon, 654 pp.
- Eriksen, C. C., 1980: Evidence for a continuous spectrum of equatorial waves in the Indian Ocean. *J. Geophys. Res.*, **85**, 3285–3303, https://doi.org/10.1029/JC085iC06p03285.
- —, 2017a: Physical data collected from Seaglider SG035 during Bermuda / Hydrostation S / BATS 20 March 2014 in the NW Atlantic deployed from 2014-03-20 to 2014-06-17 (NCEI Accession 0162366). NCEI NOAA Archive, accessed 1 March 2021, https://www.ncei.noaa.gov/archive/archive-management-system/OAS/bin/prd/jquery/accession/det ails/162366.
- ——, 2017b: Physical data collected from Seaglider SG035 during Bermuda / Hydrostation S / BATS 30 January 2015 in the NW Atlantic deployed from 2015-01-30 to 2015-11-05 (NCEI accession 0162319). NCEI NOAA Archive, accessed 1 March 2021, https:// www.ncei.noaa.gov/archive/archive-management-system/OAS/bin/ prd/jquery/accession/details/162319.
- ——, 2017c: Water temperature and salinity profiles from CTD taken from Seaglider 037, Seaglider 038, and Seaglider 039 in the coastal North Atlantic from 2017-04-08 to 2018-11-21 (NCEI accession 0209067). NCEI NOAA Archive, accessed 1 March 2021, https://www.ncei.noaa.gov/archive/archive-mana gement-system/OAS/bin/prd/jquery/accession/details/209067.
- ——, 2021: Water temperature, salinity, and others collected from Seagliders SG041 and SG045 in the North Atlantic Ocean from 2018-09-05 to 2019-11-25 (NCEI accession 0233436). NCEI NOAA Archive, accessed 1 July 2021, https://www.ncei.noaa.gov/archive/accession/0233436.
- —, T. J. Osse, R. D. Light, T. Wen, T. W. Lehman, P. L. Sabin, J. W. Ballard, and A. M. Chiodi, 2001: Seaglider: A long-range autonomous underwater vehicle for oceanographic research. *IEEE J. Oceanic Eng.*, 26, 424–436, https://doi.org/10.1109/48.972073.
- Flierl, G. R., 1978: Models of vertical structure and the calibration of two-layer models. *Dyn. Atmos. Oceans*, 2, 341–381, https:// doi.org/10.1016/0377-0265(78)90002-7.
- Fu, L., and G. Flierl, 1980: Nonlinear energy and enstrophy transfers in a realistically stratified ocean. *Dyn. Atmos. Oceans*, 4, 219–246, https://doi.org/10.1016/0377-0265(80)90029-9.
- Garrett, C., and W. Munk, 1979: Internal waves in the ocean. Ann. Rev. J. Fluid Mech., 11, 339–369, https://doi.org/10.1146/annurev.fl.11.010179.002011.
- Hua, B., and D. Haidvogel, 1986: Numerical simulations of the vertical structure of quasi-geostrophic turbulence. *J. Atmos. Sci.*, 43, 2923–2936, https://doi.org/10.1175/1520-0469(1986)043<2923: NSOTVS>2.0.CO:2.
- Jackett, D. R., and T. McDougall, 1997: A neutral density variable for the world's oceans. J. Phys. Oceanogr., 27, 237–263, https:// doi.org/10.1175/1520-0485(1997)027<0237:ANDVFT>2.0.CO;2.
- Kjellsson, J., and L. Zanna, 2017: The impact of horizontal resolution on energy transfers in global ocean models. *Fluids*, 2, 45, https://doi.org/10.3390/fluids2030045.
- Kolmogorov, A., 1941: The local structure of turbulence in incompressible viscous fluids for very large Reynolds numbers. Dokl. Akad. Nauk SSSR, 30, 301–304.

- Kraichnan, R., 1967: Inertial ranges in two-dimensional turbulence. *Phys. Fluids*, **10**, 1417–1423, https://doi.org/10.1063/1.1762301.
- LaCasce, J., 2017: The prevalence of oceanic surface modes. *Geophys. Res. Lett.*, 44, 11 097–11 105, https://doi.org/10.1002/2017GL075430.
- Lapeyre, G., and P. Klein, 2006: Dynamics of the upper oceanic layers in terms of surface quasi-geostrophic theory. J. Phys. Oceanogr., 36, 165–176, https://doi.org/10.1175/JPO2840.1.
- McDougall, T., and P. Barker, 2011: Getting started with TEOS-10 and the Gibbs Seawater (GSW) Oceanographic Toolbox. SCOR/IAPSO WG127, 28 pp., https://www.teos-10.org/pubs/ Getting\_Started.pdf.
- McWilliams, J. C., 1989: Statistical properties of decaying geostrophic turbulence. J. Fluid Mech., 198, 199–230, https://doi.org/10.1017/S0022112089000108.
- —, and Coauthors, 1983: The local dynamics of eddies in the western North Atlantic. *Eddies in Marine Science*, Springer-Verlag, 92–113.
- Munk, W., 1981: Internal waves and small scale processes. The Evolution of Physical Oceanography: Scientific Papers in Honor of Henry Stommel, B. A. Warren and C. Wunsch, Eds., MIT Press, 264–291.
- Oort, A., S. Ascher, S. Levitus, and J. Peixoto, 1989: Available potential energy in the world ocean. J. Geophys. Res., 94, 3187, https://doi.org/10.1029/JC094iC03p03187.
- Pelland, N., C. Eriksen, and C. Lee, 2013: Subthermocline eddies over the Washington continental slope as observed by Seagliders. J. Geophys. Res. Oceans, 43, 2025–2053, https://doi. org/10.1175/JPO-D-12-086.1.
- Qiu, B., S. Chen, P. Klein, H. Sasaki, and Y. Sasai, 2014: Seasonal mesoscale and submesoscale eddy variability along the North Pacific subtropical countercurrent. *J. Phys. Oceanogr.*, 44, 3079–3098, https://doi.org/10.1175/JPO-D-14-0071.1.
- —, —, J. Wang, H. Torres, L. Fu, and D. Menemenlis, 2018: Seasonality in transition scale from balanced to unbalanced motions in the world ocean. *J. Phys. Oceanogr.*, 48, 591–605, https://doi.org/10.1175/JPO-D-17-0169.1.
- Rhines, P., 1979: Geostrophic turbulence. Annu. Rev. Fluid Mech., 11, 401–441, https://doi.org/10.1146/annurev.fl.11.010179.002153.
- Ruan, X., J. O. Wenegrat, and J. Gula, 2021: Slippery bottom boundary layers: The loss of energy from the general circulation by bottom drag. *Geophys. Res. Lett.*, 48, e2021GL094434, https://doi.org/10.1029/2021GL094434.
- Scott, R., and F. Wang, 2005: Direct evidence of an oceanic inverse energy cascade from satellite altimetry. J. Phys. Oceanogr., 35, 1650–1666, https://doi.org/10.1175/JPO2771.1.
- Smith, S., and G. Vallis, 2001: The scales and equilibrium of midocean eddies: Freely evolving flow. J. Phys. Oceanogr., 31, 554–571, https://doi.org/10.1175/1520-0485(2001)031<0554: TSAEOM>2.0.CO;2.
- —, and R. Ferarri, 2009: The production and dissipation of compensated thermohaline variance by mesoscale stirring. *J. Phys. Oceanogr.*, 39, 2477–2501, https://doi.org/10.1175/2009JPO4103.1.
- Steinberg, J., and C. Eriksen, 2020: Glider sampling simulations in high resolution ocean models. *J. Atmos. Oceanic Technol.*, **37**, 975–992, https://doi.org/10.1175/JTECH-D-19-0200.1.
- Tozer, B., D. Sandwell, W. Smith, C. Olson, J. Beale, and P. Wessel, 2019: Global bathymetry and topography at 15 arc sec: SRTM15+. Earth Space Sci., 6, 1847–1864, https://doi.org/10.1029/2019EA000658.
- Tulloch, R., J. Marshall, and K. Smith, 2009: Interpretation of the propagation of surface altimetric observations in terms of planetary waves and geostrophic turbulence. *J. Geophys. Res.*, 114, C02005, https://doi.org/10.1029/2008JC005055.

- Vallgren, A., and E. Lindborg, 2010: Charney isotropy and equipartition in quasi-geostrophic turbulence. *J. Fluid Mech.*, 656, 448–457, https://doi.org/10.1017/S0022112010002703.
- Vallis, G., 2006: Atmosphere and Oceanic Fluid Dynamics: Fundamentals and Large-Scale Circulation. Cambridge University Press, 745 pp.
- von Storch, H., and F. W. Zwiers, 2003: Statistical Analysis in Climate Research. 2nd ed. Cambridge University Press, 484 pp.
- Wunsch, C., 1997: The vertical partition of oceanic horizontal kinetic energy. *J. Phys. Oceanogr.*, **27**, 1770–1794, https://doi.org/10.1175/1520-0485(1997)027<1770:TVPOOH>2.0.CO;2.
- Xu, Y., and L. Fu, 2010: Global variability of the wavenumber spectrum of oceanic mesoscale turbulence. J. Phys. Oceanogr., 41, 802–809, https://doi.org/10.1175/2010JPO4558.1.
- —, and —, 2012: The effects of altimeter instrument noise on the estimation of the wavenumber spectrum of sea surface height. *J. Phys. Oceanogr.*, **42**, 2229–2233, https://doi.org/10.1175/JPO-D-12-0106.1.
- Zhao, M., M. Timmermans, R. Krishfield, and G. Manucharyan, 2018: Partitioning of kinetic energy in the Arctic Ocean's Beaufort Gyre. *J. Geophys. Res. Oceans*, **123**, 4806–4819, https://doi.org/10.1029/2018JC014037.